Top quark phenomena in association with new vector bosons

Bilguun Bayarsaikhan, Tsedenbaljir Enkhbat,*

Lkhagvadorj Erdenebulgan, and Zorigoo Lkhamjav

Institute of Physics and Technology, Mongolian Academy of Science,

Peace avenue 54b, Ulaanbaatar 13330, Mongolia and

†Nuclear Research Center, National University of Mongolia,

University street 1, Ulaanbaatar 14200, Mongolia

We study collider phenomenology of pair produced new heavy vector bosons further decaying into top pair plus bottom pair production in proton-proton collisions at CERN LHC with 13 TeV center of mass energy in the presence of new color octet vector boson. While the final signal is challenging to study due to high number of jets and combinatirocal background, it nevertheles presents an ample opportunity to explore due to large production cross-section and energetic jets. We show that the the invariant mass of the leading two jets and the leading b-jet p_T distribution can be used to distinguish the signal from the Standard model background efficiently.

I. INTRODUCTION

The Standard Model (SM) of particle physics has been very successful in explaining the particle physics phenomena. Still there are questions that are not adequately addressed in the SM. These include baryon antibaryon asymmetry, neutrino oscillations and in some extent the scale of electroweak symmetry breaking. Currently the only experiments that may shed light on these questions are the LHC up to 14 TeV center of mass energy. One of the leading hypothesis on the baryon asymmetry of the universe is the electroweak baryogenesis. The requirement of this frame work is that the electroweak phase transition from symmetric state to spontaneously broken one should be strongly first order and to do so one must have: $\phi_c/T_c \gtrsim O(1)$, where ϕ_c is the vacuum expectation value of the Higgs field at the critical temperature T_c of the thermal bath. Unfortunately, it does not work in the SM where it implies the Higgs

---

*enkhbat@ipt.ac.mn

mass to be 70 GeV which is in a direct conflict with the measured value by ATLAS and CMS collaborations at the LHC [1]. Therefore new particles which modify the Higgs potential through quantum corrections or new shape for the Higgs potential are needed. Colored particles within the reach of the LHC experiments are one such possibility [2]. In doing so, Higgs pair production can be modified substantially See for example [3–6]).

In the present work, we study the phenomenology of pair produced new heavy vector bosons with color quantum numbers. The decay channels we examine are the pair produced heavy vector bosons that dominantly decay into third generation quarks. If the new vector boson has a negligible coupling to light generation a single vector boson via quark-antiquark fusion is not the leading prodcution mechanism. Instead the gluon fusion induced pair production becomes dominant since a massive single vector particle cannot be produced from two massless vector bosons due to the Landau-Yang theorem. The production of a single leptoquark is through coupling to the light generations and therefore highly model dependent. The analysis of such events are quite complicated and in the current work we present (i) identification of one them by their decay products, (ii) top and bottom quark event simulation for 13 TeV center of mass energy at the LHC. In the final part we present prelimenary results of the top and bottom quark signals at the detector level.

II.   PAIR OF NEW VECTOR BOSONS

A.   Analysis

For our analysis we use Madgraph 5 [8], a matrix element generator that simulates high energy proton-proton collision at the CERN-LHC. We use Feynrule software [7] to have a Madgraph implementable model file . Feynrule is a Mathematica package in which user provides the Lagrangian of the model under the consideration. If it is properly implemented the Feynrule package generates all the necessary Feynman rules for the model (such as the SM and its extension) in the UFO format that can be readily used in the Madgraph5 environment. The Lagrangian of our model is as follows:

$$\mathcal{L} = \mathcal{L}_{SM} - \frac{1}{4}V^{a\mu\nu}V_{a\mu\nu} + g_{fij}\bar{f}_i\gamma^\mu t^a V_{a\mu}f_j, \tag{1}$$

where V_μ is the new color–octet heavy vector boson.

In order to simulate the full process in Madgraph5, we use Pythia 8-hadron showering [9] and Delphes detector simulation tools [10], where the latter two are integrated within Madgraph5 environment. The steps of our computation are given as follows:

First step: Matrix level

Matrix elements of our events are calculated using the MadGraph5. The invariant mass distribution of matrix level top pair production at the LHC is shown Figure(1).
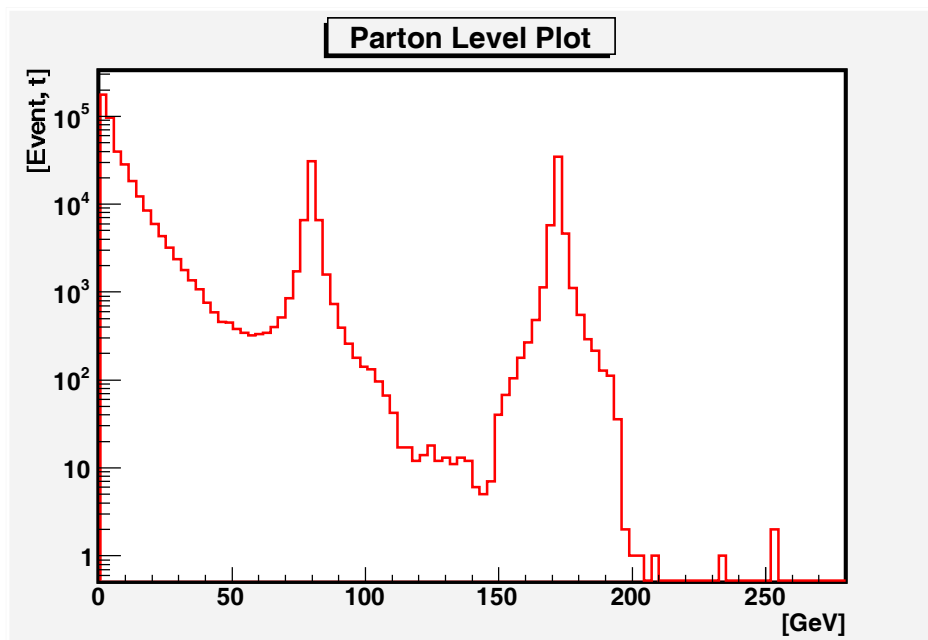

FIG. 1: Result of matrix level

Second step: Parton level

Using the results of matrix element, hadron showering is done by Pythia. The Pythia provides the results in the CERN root file format.

Third step: Detector level

To seperate our events from the SM background we use suitable kinematic cuts. Finally, the latest results are processed using CERN-ROOT program.

B.   Event selection strategy

We first discuss four-jet decay channel, where our signal process is $VV^* \to b\bar{b}b\bar{b}jjjj$. Jets are clustered using anti-k_T algorithm[12] with $R = 0.5$ and we require jets to have $p_T > 50$GeV and $|eta| < 4.9$.

Events must have at least 4 jetsee, at least one of which must be b-tagged. The leading b-tagged and light jets must have $p_T \geq 250$ GeV, and the subleading light jet must have $p_T \geq 80$ GeV. Furthermore, the signal mass is optimized by the scalar sum paramter $H_T = \sum_j |p_{T,j}| \geq \frac{4}{3}m_V$[11].

We have to reconstruct final decay products in order to study new vector boson decay. There are three main steps to reconstruct.

- Two jets have been reconstructed to yeald a W boson candidate and the result is displayed in Figure 2.

- Three jets (including W boson plus b jet) have been reconstructed to yeald top quark candidate that is showed in Figure 3.

- Finally, the four jets (including top quark plus leading b jet) have been used for reconstructing the vector boson candidate.
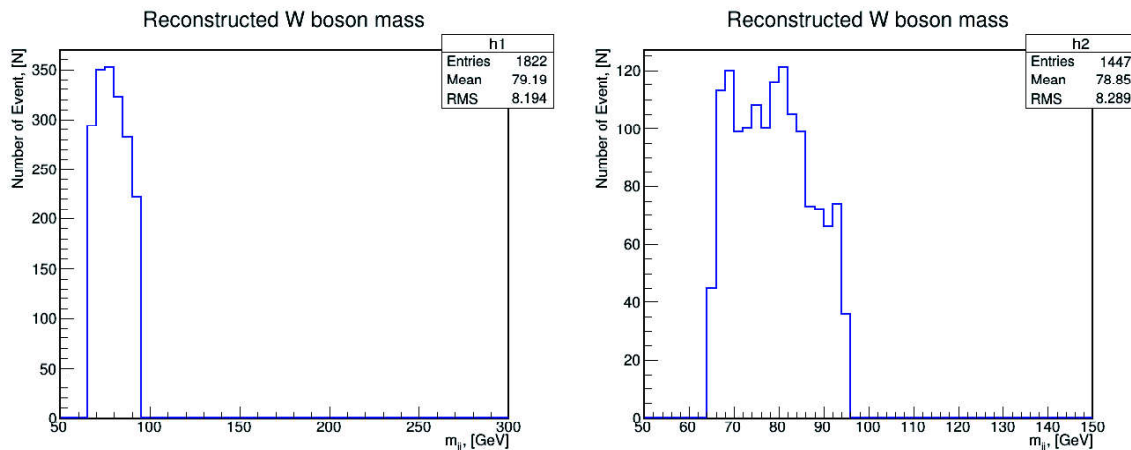

FIG. 2: Reconstruction of W boson candidate

In order to reconstruct W boson, we need to choose the mass range ($65 \leq m_{jj} \leq 95$) around the W boson mass value. In addition we reconstruct top quark events using the previously reconstructed W boson candidate with b-jet candidates. There are totally 12 combinations, but we displayed only 2 combination here as an example.
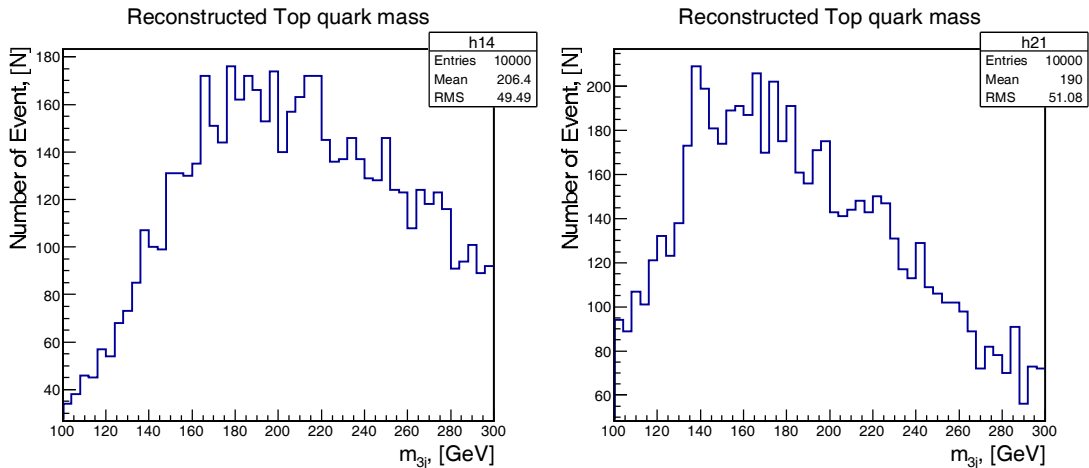
FIG. 3: Reconstruction of Top quark candidate

These results are shown in Figure 2 and Figure 3. When the reconstructed top quark mass result is compared to that of the CMS result[1], it is clear that we have to improve kinematic cuts and find matching jets correctly. This is mainly due to large combinatoric background, which may lead to permutations of jets that give a false signal accidentally. This background is very difficult to suppress in general. On the other hand, the case of boosted top production the situation is comparatively simpler, since double and triple jets from the boosted top quark and W boson candidates are identified as single jet in the detector. Therefore, we only need to consider leading and sub-leading b-tagged and light jets. The reconstructed results from these leading and sub-leading jets are shown in Figure 4. As we can see, in this case, top quark and W boson are reconstructed in a much clean manner.
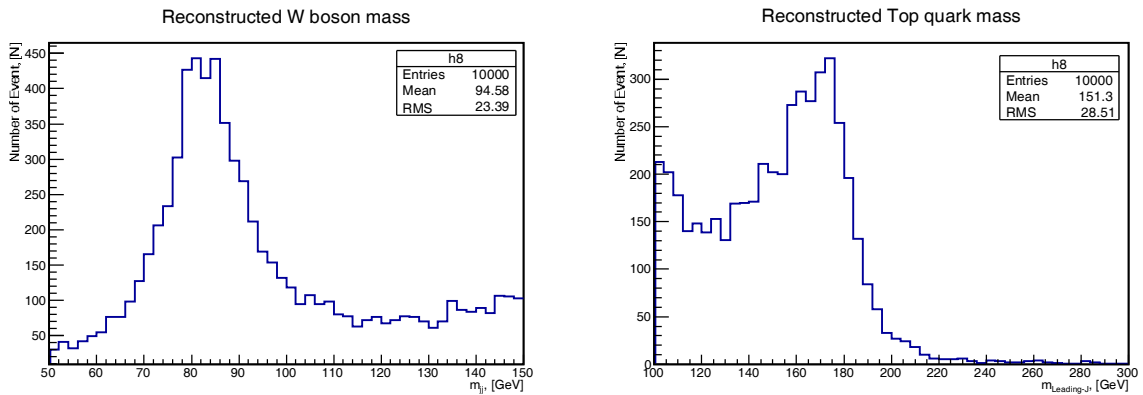

FIG. 4: Reconstruction of W boson and top quark with leading jet.

<center>### C.   New vector boson production</center>

First, we perform a simulation at hadron level, where we choose the new vector boson mass to be $M_V = 700$ GeV and it is in $SU(3)$ color octet representation. The hadron level result with such vector boson extension is shown in Figure 5.
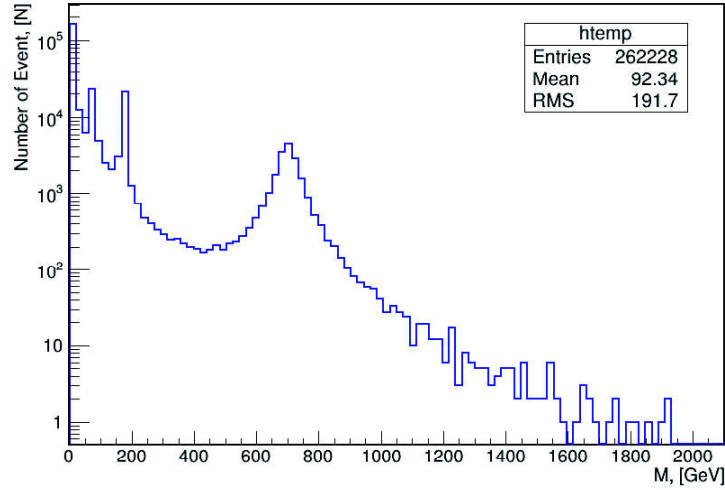

<center>FIG. 5: Hadron level result of vector boson</center>

We have scanned by the mass of the new vector boson and the results are shown as the cross–section versus the vector boson mass. The results for charged particle production cross-section and its decay to top and bottom quarks are shown in Figure 6. The neutral case is shown in Figure 7.
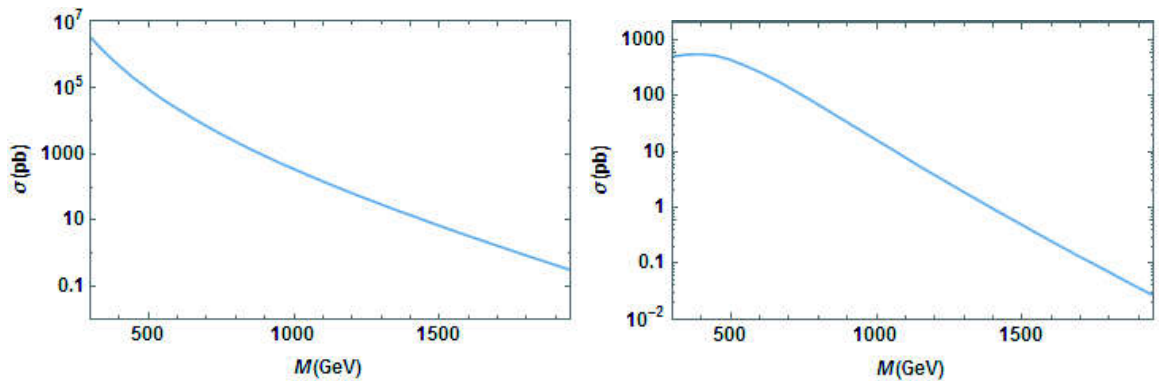

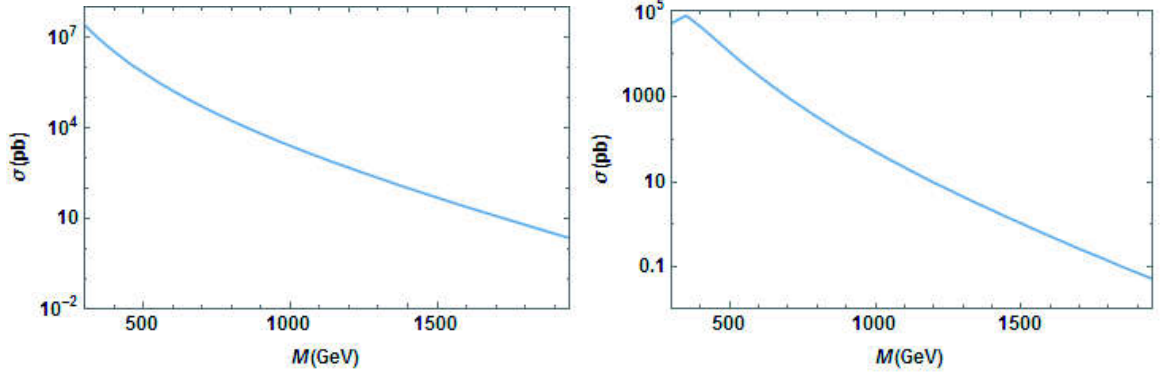FIG. 6: Production Cross-section and decay to t, b quarks at the matrix level for charged vector boson

FIG. 7: Production Cross-section and decay to t, $\bar{t}$ quarks at the matrix level for neutral heavy boson.

Consideration of b-tagged jet PT is shown in Figure 8 with the SM and the extended SM. SM leading b-jets PT is dramatically decreasing as energy range is increasing. In our model, leading b-jet PT is different than SM. It is a interesting phenomenology to check new vector boson at the LHC, only using leading b-jets PT.
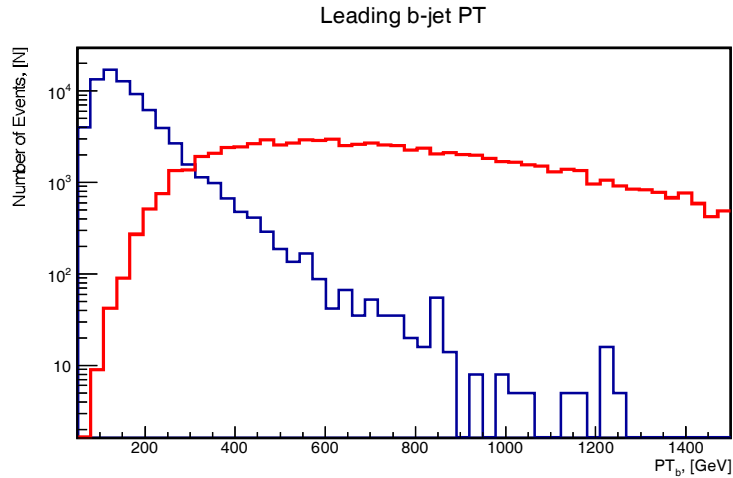

FIG. 8: Leading b-jet PT in SM compared to the extended SM.

In the SM, top-bottom, two b-tagged and two light jet invariant mass distribution is shown in Figure 9 compared with case of new vector boson decay to top and bottom quark. It is clear that, from mass range of 500 GeV, event number is increased significantly, and there is possibility to check this scenario at the LHC experiments.
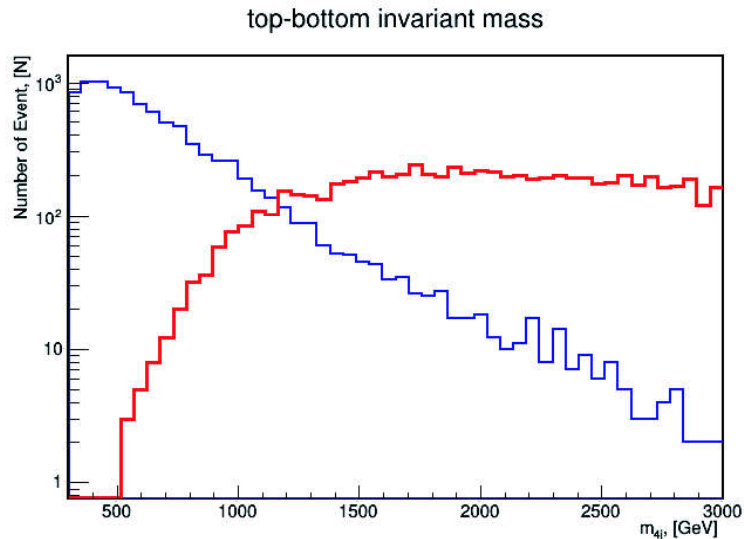
FIG. 9: Invariant mass of top-bottom quark candidate in SM compared to the extended SM.

III.   CONCLUSION

In the current paper, we have presented our study on the production of new vector boson pairs at the LHC and their decay to the third generation quarks. As an example we have chosen the results from the top and bottom quark. In our extended SM, we have shown that a new color octet vector boson, that is predicted to exist in number of SM extendedmodels possible to measure at the LHC.

Acknowledgments

[1] *Measurements of top-quark pair differential cross-sections in the eμ channel in pp collisions at $\sqrt{s} = 13 TeV$ using the ATLAS detector*, arXiv:1612.05220

[2] E. H. Simmons, Phys. Rev. D **55**, 1678 (1997) doi:10.1103/PhysRevD.55.1678 [hep-ph/9608269].

[3] A. Belyaev, M. Drees, O. J. P. Eboli, J. K. Mizukoshi and S. F. Novaes, Phys. Rev. D **60** (1999) 075008 doi:10.1103/PhysRevD.60.075008 [hep-ph/9905266].

[4] E. Asakawa, D. Harada, S. Kanemura, Y. Okada and K. Tsumura, Phys. Rev. D **82** (2010) 115002 doi:10.1103/PhysRevD.82.115002 [arXiv:1009.4670 [hep-ph]].

[5] G. D. Kribs and A. Martin, Phys. Rev. D **86** (2012) 095023 doi:10.1103/PhysRevD.86.095023 [arXiv:1207.4496 [hep-ph]].

[6] Ts. Enkhbat: *Higgs pair production from color octet scalars and vectors*, arXiv: 1504.08305v1

[7] Adam Alloul, Neil D. Christensen, Celine Degrande, Claude Duhr, Benjamin Fuks : *FeynRules 2.0 - A complete toolbox for tree-level phenomenology*, arXiv:1310.1921

[8] Johan Alwall, Michel Herquet, Fabio Maltoni, Olivier Mattelaer, Tim Stelzer : *Mad-Graph 5 : Going Beyond*, arXiv:1106.0522v1

[9] Torbjorn Sjostrand, Stephen Mrenna, Peter Skands : *PYTHIA 6.4 Physics and Manual*, arXiv:hep-ph/0603175

[10] J. de Favereau, C. Delaere, P. Demin, A. Giammanco, V. Lematre, A. Mertens, M. Selvaggi : *DELPHES 3, A modular framework for fast simulation of a generic collider experiment*

[11] Malte Buschmann and Felix Yu : *Collider constraints and new tests of color octet vectors*, arXiv:1706.07057v1

[12] Matteo Cacciari, Gavin P. Salam, and Gregory Soyez : *The Anti-k(t) jet clustering algorithm*, JHEP 04, 063(2008), arXiv:0802.1189[hep-ph]

Decomposed Photodisintegration Cross Section of ^{9}Be in the Complex Scaling Method

Myagmarjav Odsuren,* Gonchigdorj Khuukhenkhuu, and Suren Davaa

School of Engineering and Applied Sciences,
National University of Mongolia, Ulaanbaatar 210646, Mongolia and
Nuclear Research Center, National University of Mongolia, Ulaanbaatar 210646, Mongolia

Kiyoshi Katō

Nuclear Reaction Data Centre, Faculty of Science,
Hokkaido University, Sapporo 060-0810, Japan

(Dated: March 13, 2018)

We investigate the decomposed photodisintegration cross section for the ^{9}Be($1/2^+$) state, which is important to realize the properties of the unbound $1/2^+$ state of ^{9}Be. The recent experimental data are discussed to be explained by an $\alpha + \alpha + n$ model. In order to calculate the photodisintegration cross section into $\alpha + \alpha + n$ three-body final states, the complex scaling method is used.

I. INTRODUCTION

The complex scaling method (CSM) [1–5] is a well-established technique in wide areas of physics especially in areas of resonance studies in nuclear physics. At the beginning, its advantage was mainly explained by the superior description of the resonance states of composite systems. Nowadays, it is successfully utilized for getting information of unbound and scattering states.

We apply the CSM to an $\alpha + \alpha + n$ three-cluster model to understand the structure and (γ, n) reaction for low-lying states in ^{9}Be. For the purpose of this work we investigate the unbound nature of the $1/2^+$ state of ^{9}Be and study the decomposed photodisintegration cross section between the excited $1/2^+$ and ground $3/2^-$ states. In this study, we discuss the recent experimental data [6, 7] of the photodisintegration cross section and structure of the $1/2^+$ state in the ^{9}Be system.

---

*odsuren@seas.num.edu.mn

II. METHOD

The Schrödinger equation is solved by utilizing the orthogonality condition model (OCM) [8] for the $\alpha + \alpha + n$ (^{9}Be) three-body system as following

$$H\Psi^\nu_{J\pi} = E_\nu \Psi^\nu_{J\pi}, \tag{1}$$

where J^π is the total spin and parity of the $\alpha + \alpha + n$ system and ν is the state index. The complex-scaled Schrödinger equation is given as

$$\hat{H}^\theta \Psi^\nu_J(\theta) = E^\theta_\nu \Psi^\nu_J(\theta). \tag{2}$$

The complex-scaled Hamiltonian and wave function are given as

$$\hat{H}^\theta = U(\theta)\hat{H}U^{-1}(\theta) \quad \text{and} \quad \Psi^\nu_J(\theta) = U(\theta)\Psi^\nu_J, \tag{3}$$

respectively. The complex scaling operator $U(\theta)$ transforms the relative coordinate $\boldsymbol{\xi}$ as

$$U(\theta) : \boldsymbol{\xi} \to \boldsymbol{\xi} e^{i\theta}, \tag{4}$$

where θ is the scaling angle being a positive real number.

The Hamiltonian for the relative motion of the $\alpha + \alpha + n$ three-body system for ^{9}Be is given as

$$\hat{H} = \sum_{i=1}^{3} t_i - T_{\text{c.m.}} + \sum_{i=1}^{2} V_{\alpha n}(\boldsymbol{\xi}_i) + V_{\alpha\alpha} + V_{\text{PF}} + V_3, \tag{5}$$

where t_i and $T_{\text{c.m.}}$ are kinetic operators for each particle and the center-of-mass of the system, respectively. The interactions between the neutron and the i-th α particle is given as $V_{\alpha n}(\boldsymbol{\xi}_i)$, where $\boldsymbol{\xi}_i$ is the relative coordinate between them. We here employ the KKNN potential [9] for $V_{\alpha n}$. For the α-α interaction $V_{\alpha\alpha}$ we employ a folding potential of the effective NN interaction [10] and the Coulomb interaction:

$$V_{\alpha\alpha}(r) = v_0 \exp\left(-ar^2\right) + \frac{4e^2}{r}\text{erf}\left(\beta r\right), \tag{6}$$

where $v_0 = -106.09$ MeV, $a = 0.2009$ fm^{-2}, and $\beta = 0.5972$ fm^{-1}. The pseudo potential $V_{\text{PF}} = \lambda|\Phi_{PF}\rangle\langle\Phi_{PF}|$ is the projection operator to remove the Pauli forbidden states from the relative motions of α-α and α-n [8, 11]. The Pauli forbidden state is defined as the harmonic oscillator wave functions by assuming the $(0s)^4$ configuration whose oscillator length is fixed to reproduce the observed charge radius of the α particle. In the present calculation, λ is taken as 10^6 MeV.

To discuss the photodisintegration of ^{9}Be, it is important to reproduce the breakup threshold into the $\alpha + \alpha + n$ system. In the present calculation, we introduce the $\alpha + \alpha + n$ three-body potential V_3 to reproduce the binding energy of the ^{9}Be ground state, E_{gs}, measured from the $\alpha + \alpha + n$ threshold. The explicit form of V_3 is given as

$$V_3 = v_{3b} \exp\left(-\mu\rho^2\right), \tag{7}$$

where ρ is the hyper-radius of the $\alpha + \alpha + n$ system.

We solve the eigenvalue problem given in Eq. (2) with Gaussian expansion method [12], and obtain the energy eigenvalues and eigenstates (their biorthogonal states) as $\{E_\nu^\theta\}$ and $\{\Psi_J^\nu(\theta)\}$ ($\{\tilde{\Psi}_J^\nu(\theta)\}$), respectively. Using them, we define the complex-scaled Green's function $\mathcal{G}^\theta(E;\boldsymbol{\xi},\boldsymbol{\xi}')$ as

$$\mathcal{G}^\theta(E;\boldsymbol{\xi},\boldsymbol{\xi}') = \left\langle \boldsymbol{\xi} \left| \frac{1}{E - H^\theta} \right| \boldsymbol{\xi}' \right\rangle = \sum_\nu \!\!\!\!\!\!\int \frac{\Psi^\nu(\theta)\tilde{\Psi}^\nu(\theta)}{E - E_\nu^\theta}. \tag{8}$$

In the derivation of the right-hand side of Eq. (8), we use the extended completeness relation, whose detailed explanation is given in Ref. [13–15]. It is noticed that we take into account outgoing boundary conditions for all open channels of a three-body system in the form of complex energy eigenvalues E_ν^θ. The complex-scaled Green's function in Eq. (8) enables us to describe the scattering observables for many-body systems, such as the photodisintegration cross section.

We calculate the cross section of the photodisintegration of ^{9}Be($3/2^-$) $+ \gamma \rightarrow \alpha + \alpha + n$ in terms of the multipole response. The cross section is expressed as the following form;

$$\sigma_{E\lambda}^\gamma(E_\gamma) = \frac{(2\pi)^2(\lambda+1)}{\lambda[(2\lambda+1)!!]^2}\left(\frac{E_\gamma}{\hbar c}\right)^{2\lambda-1}\frac{dB(E\lambda, E_\gamma)}{dE_\gamma}, \tag{9}$$

where E_γ is the incident photon energy and $B(E\lambda)$ is electric transition strength with the rank λ. We here calculate the photodisintegration cross section from the ground $3/2^-$ state to $1/2^+$ states in ^{9}Be and consider only the $E1$ transition. Using the CSM and the complex-scaled Green's function in Eq. (8), the $E1$ transition strength is given as

$$\frac{dB(E1, E_\gamma)}{dE_\gamma} = \frac{1}{2J_{\mathrm{gs}}+1}\sum_\nu \!\!\!\!\!\!\int \left\langle \tilde{\Psi}_{\mathrm{gs}}||(\hat{O}^\theta)^\dagger(E1)||\Psi_{1/2^+}^\nu(\theta) \right\rangle$$
$$\times \frac{1}{E - E_\nu^\theta}\left\langle \tilde{\Psi}_{1/2^+}^\nu(\theta)||\hat{O}^\theta(E1)||\Psi_{\mathrm{gs}} \right\rangle, \tag{10}$$
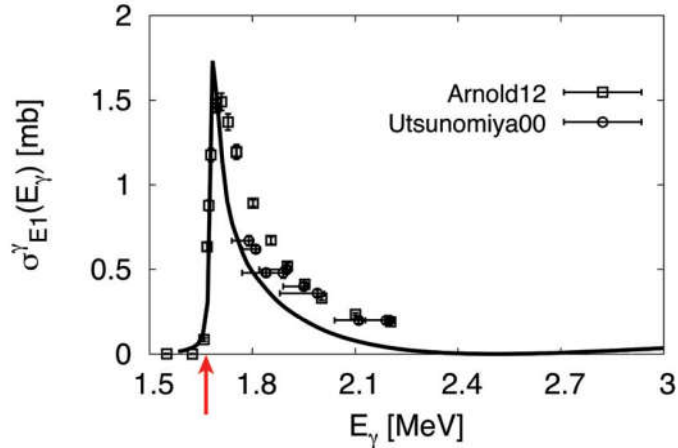
FIG. 1: Calculated photodisintegration cross section of ^{9}Be in comparison with the experimental data. The black (solid) line represents the cross section calculated by using an attractive three-body potential with $v_{3b} = -17$ MeV. The experimental data below $E_\gamma = 2.2$ MeV are taken from Refs. [6] and [7]. The arrow indicates the threshold energy of the ^{8}Be(0^+) $+ n$ channel.

where J_{gs} and Ψ_{gs} represent the total spin and the wave function of the ground state, respectively. The energy E is related to E_γ as $E = E_\gamma - E_{\mathrm{gs}}$. From the Eqs. (9) and (10), we finally obtain the photodisintegration cross section as

$$\sigma_{E1}^\gamma(E_\gamma) = \frac{16\pi^3}{9\hbar c} E_\gamma \frac{dB(E1, E_\gamma)}{dE_\gamma}. \tag{11}$$

III. RESULTS AND DISCUSSIONS

The CSM has been utilized to investigate the ^{9}Be($1/2^+$) state [16–19]. But in the previous works, the $3/2^-$ ground state of ^{9}Be is calculated as 2.16 MeV from the $\alpha + \alpha + n$ threshold without three-body potential. The KKNN [9] and folding [10] potentials are effective potentials for $\alpha + n$ and $\alpha + \alpha$, respectively, which reproduce well the experimental data in the low energy region and it is widely applied in the analysis of two- or three-body systems.

In the present calculation, we fix the ground-state wave function obtained with the three-body potential with $v_{3b} = 6.57$ MeV and $\mu = 0.1$ fm^{-2} in Eq. (7) to reproduce the experimental binding energy of the ground state as 1.574 MeV measured from the three-body threshold [10]. In FIG. 1, we show the calculated cross section using Eq. (11) in comparison with the two sets of the observed data which commonly have peaks just above the ^{8}Be $+ n$ threshold.

To discuss the observed sharp peak just above the $^8Be + n$ threshold in the photodisintegration cross section, we change the strength, v_{3b}, for the $1/2^+$ state to fit the observed data but its range is fixed as the same as used in the ground state. We here take the strength as $v_{3b} = -17$ MeV for the $1/2^+$ state and obtain the cross section as shown as the black (solid) line in Fig. 1. Our result reproduces the observed peak by using the attractive three-body potential. It is seen that the calculated cross section rapidly increases just above the $^8Be + n$ threshold and there is negligibly small strength below this threshold.

We investigate the origin of the low-lying peak above the $^8Be + n$ threshold in detail. For this purpose, we show the distribution of the energy eigenvalues of the $^9Be(1/2^+)$ states obtained by using the CSM in Fig. 2. In the CSM, continuum states are obtained along the branch cuts which start from the threshold energies and are rotated down by 2θ. A resonance is obtained as a solution with complex energy of $E^\theta = E_r - i\Gamma/2$ isolated from the continuum ones. On the other hand, the virtual states and broad resonances, which are located on the second Riemann sheet covered by the rotated first Riemann sheet, cannot be obtained as the isolated pole in CSM. The contributions from these states to the cross section are scattered into the continuum states rotated on the 2θ lines. In Fig. 2, we show the distribution of the
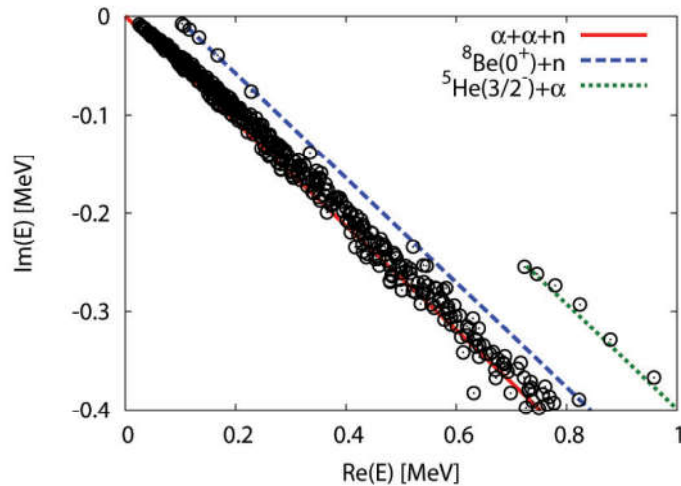

FIG. 2: Distribution of energy eigenvalues of the $^9Be(1/2^+)$ states measured from the $\alpha + \alpha + n$ threshold with scaling angle $\theta = 15$ degrees. The three-body potential with $v_{3b} = -17$ MeV and $\mu = 0.1$ fm^{-2} was employed. The red (solid), blue (dashed), and green (dotted) lines represent the branch cuts for $\alpha + \alpha + n$, $^8Be(0^+) + n$, and $^5He(3/2^-) + \alpha$ continua, respectively.
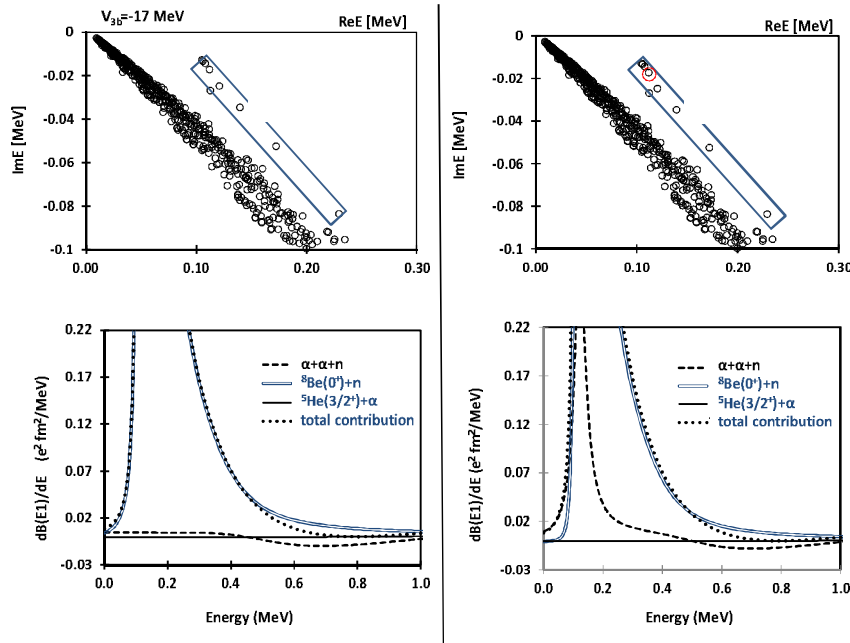
FIG. 3: The decomposition of photodisintegration cross section of the $\alpha + \alpha + n$ system. The $v_{3b} = -17$ MeV is applied. Upper panel: The distribution of eigenvalues are given in the complex energy plane. Lower panel: The decomposed photodisintegration cross section corresponding to the branch cuts for the $\alpha + \alpha + n$, $^8\text{Be}(0^+) + n$ and $^5\text{He}(3/2^-) + \alpha$ continuum states are shown.

energy eigenvalues for the $^9\text{Be}(1/2^+)$ states calculated with $v_{3b} = -17$ MeV, which reproduces the observed peak as shown in Fig. 1. In the present calculation, we find no resonances in the energy eigenvalue distribution. All energy eigenvalues are located on the 2θ-lines, corresponding to the branch cuts for the $\alpha + \alpha + n$, $^8\text{Be}(0^+) + n$, and $^5\text{He}(3/2^-) + \alpha$ continuum states. Comparing the calculated photodisintegration cross section of the $^9\text{Be}(1/2^+)$ state with the recent new experiments [6, 7], we find that $v_{3b} = -17$ MeV gives a good agreement as shown in Fig. 1. From this result, it is shown that there is calculated no cross section in energies below the $^8\text{Be}+(0^+) + n$ threshold. The sharp peak of the cross section, indicates that if this peak is caused by a resonance state, its width is smaller than 0.2 MeV. However, our eigenvalue solutions of the CSM the Schrödinger equation indicate that there is no such a sharp resonance. To solve this problem, we investigate the properties of the photodisintegration cross section peak in more detail.

To solve a broad resonance or a virtual state, it is necessary to calculate by employing large values of θ. However, in the present $\alpha + \alpha + n$ calculations, it is
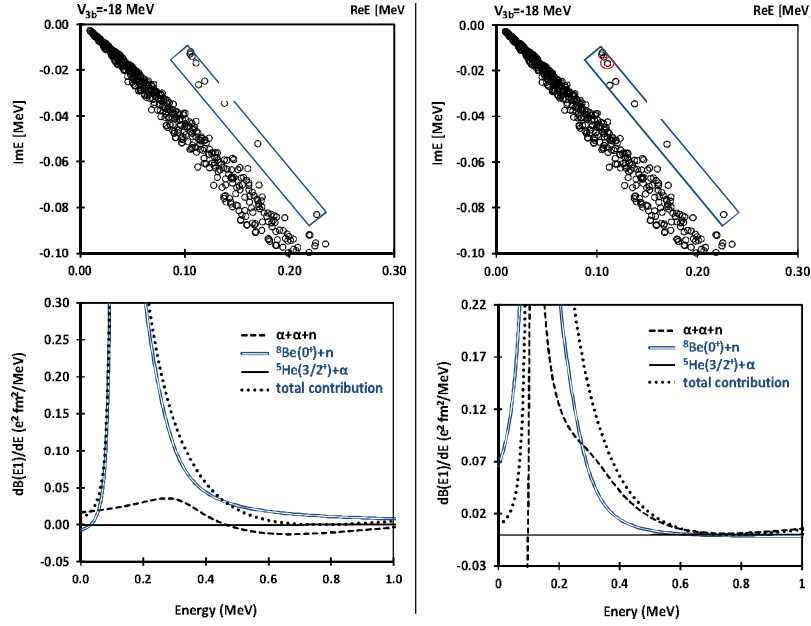
FIG. 4: The same as in Fig. 3 for $v_{3b} = -18$ MeV.
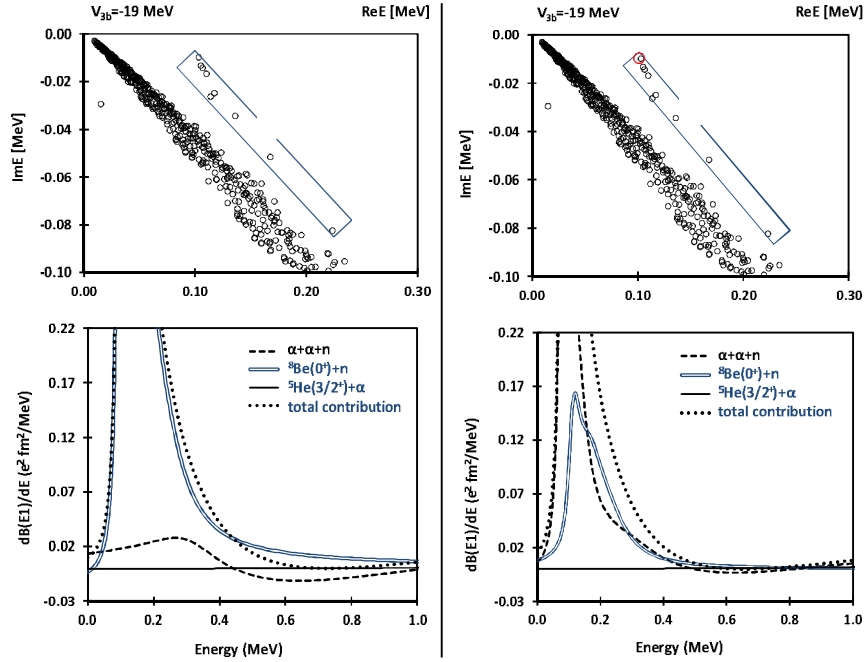
FIG. 5: The same as in Fig. 3 for $v_{3b} = -19$ MeV.

difficult to keep the numerical accuracy for a θ-value larger than $45°$. Therefore, we cannot discuss a resonances of $\Gamma > 2E_r/\sqrt{3}$ and a virtual state by applying the CSM. To overcome this problem, we investigate the decomposed photodisintegration cross section. When such a broad resonance state and a virtual state exist, it is expected
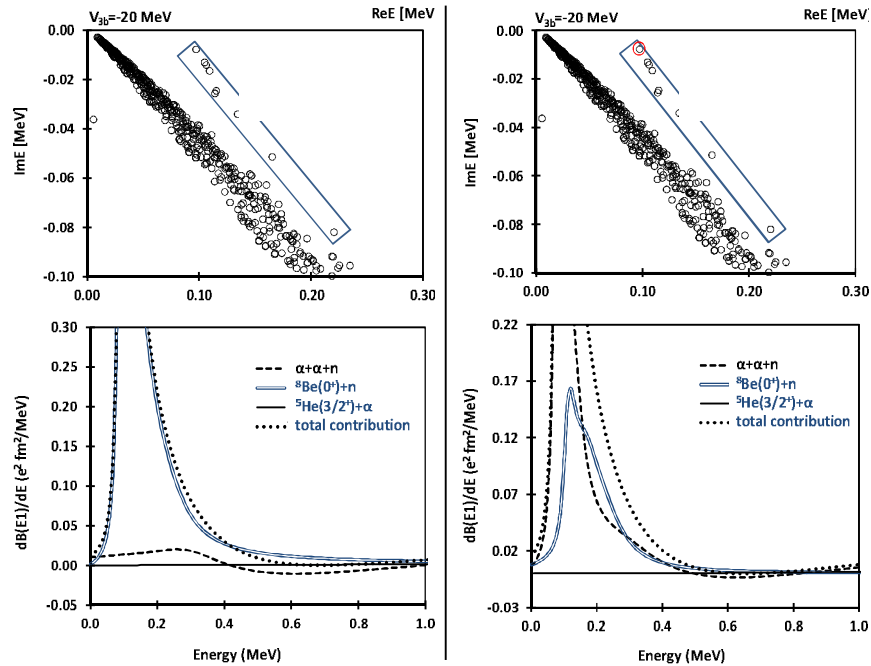
FIG. 6: The same as in Fig. 3 for $v_{3b} = -20$ MeV.

that peaks appear in the decomposed photodisintegration cross section even if they are calculated with a small value of θ.

We first check the decomposed photodisintegration cross section applying wide range values (from 30 MeV to -30 MeV) of the v_{3b} strength and look for the appropriate v_{3b} strength for the $1/2^+$ state. Then, we calculate the photodisintegration cross section using the $E1$ transition strength with $v_{3b} = -17$ MeV. Using classified eigenvalues into two- and three-body continuum states which are shown in Fig. 2, we investigate the detailed structures of the decomposed photodisintegration cross section calculated with different v_{3b} strengths. The results of the decomposed photodisintegration cross section with different v_{3b} are shown in Figs. 3—6. From lower panels of Figs. 3—6 a), it is seen that the contribution of the decomposed photodisintegration cross section for different v_{3b} from two- and three-body continuum states are shown the similar distribution with each other. We can see the contributions of the decomposed photodisintegration cross section for $v_{3b} = -17, -18, -19, -20$ MeV have a dominant component of the ^{8}Be+$(0^+) + n$ continua which is boxed in upper panels of Figs. 3—6. But the $\alpha + \alpha + n$ three-body and ^{5}He$(3/2^-) + n$ two-body continuum states do not contribute strongly.

In order to understand the ^{8}Be+$(0^+) + n$ contribution to the photodisintegration

cross section, we check contribution of each eigenstates which are boxed in the upper panels of Figs. 3–6 b). It can be seen that there is an eigenstate which gives highest contribution to the photodisintegration cross section. The eigenstate is circled in the upper panels of Figs. 3–6 b). The decomposed photodisintegration cross section by adding the eigenstate to $\alpha + \alpha + n$ three body continuum states are presented in the lower panels of Figs. 3–6 b), and we can see large differences each figures. In the case of $v_{3b} = -19$ MeV and -20 MeV, the $\alpha + \alpha + n$ three body continuum states give dominant contribution to the photodisintegration cross section. It is seen that the eigenstate contributes dominantly when we apply a deep attractive v_{3b}. This result indicate that the eigenstate have unbound characteristic.

IV.   CONCLUSION

We investigate the character of the $1/2^+$ state of ^9Be using the decomposed photodisintegration reaction with the $\alpha + \alpha + n$ three-body model and the CSM. The calculated decomposed photodisintegration cross section into the $1/2^+$ states are shown to have a strong dependence on the strength of the three-body potential for the $1/2^+$ state. From the decomposition of the calculated photodisintegration cross section, it is shown that the $^8Be + n$ continuum states dominate the photodisintegration cross section to the $1/2^+$ states. But when we apply a deep attractive potential strength to calculation of the photodisintegration cross section and to change choice of the eigenstate from two-body continuum states to three-body continuum states, $\alpha + \alpha + n$ three body continuum states give dominant contribution to the photodisintegration cross section.

[1] Y. K. Ho, Phys. Rep. **99**, 1 (1983).

[2] N. Moiseyev, Phys. Rep. **302**, 211 (1998).

[3] S. Aoyama, T. Myo, K. Katō and K. Ikeda, Prog. Theor. Phys. **116**, 1 (2006).

[4] T. Myo, Y. Kikuchi, H. Masui, and K. Katō, Prog. Part. Nucl. Phys. **79**, 1 (2014).

[5] M. Odsuren, Y. Kikuchi, T. Myo, M. Aikawa, and K. Katō, Phys. Rev. C **92**, 014322 (2015).

[6] C. W. Arnold *et al.*, Phys. Rev. C **85**, 044605 (2012).

[7] H. Utsunomiya *et al.*, Phys. Rev. C **92**, 064323 (2015).

[8] S. Saito, Prog. Theor. Phys. **40**, 893 (1968); **41**, 705 (1969); Prog. Theor. Phys. Suppl. **62**, 11(1977).

[9] H. Kanada, T. Kaneko, S. Nagata and M. Nomoto, Prog. Theor. Phys. **61**, 1327 (1979).

[10] E.W. Schmid and K. Wildermuth, Nucl. Phys. **26**, 463 (1961).

[11] A. T. Kruppa and K. Katō, Prog. Theor. Phys. **84**, 1145 (1990).

[12] E. Hiyama, Y. Kino and M. Kamimura, Prog. Part. Nucl. Phys. **51**, 223 (2003).

[13] T. Myo and K. Katō, Prog. Theor. Phys. **98**, 1275 (1997).

[14] T. Myo, K. Katō, S. Aoyama and K. Ikeda, Phys. Rev. C **63**, 054313 (2001).

[15] T. Myo, K. Katō, H. Toki, and K. Ikeda, Phys. Rev. C **76**, 024305 (2007).

[16] V. D. Efros, von P. Neumann-Cosel and A Richter, Phys. Rev. C **89** 027301 (2014).

[17] E. Gariddo, D. V. Fedorov and S. S. Jensen, Phys. Lett B **684** 132 (2010).

[18] K. Arai, P. Descouvemont, D. Baye and W. N. Catford, Phys. Rev. C **68** 014310 (2003).

[19] E. Garrido, A.S. Jensen, D.V. Fedorov, Phys. Rev. C **86**, 064608 (2012).

Tunable Magnetism of Transition Metal Nanostructures by Hydrogenated Graphene

T. Tsevelmaa[1,2], Chunfeng[3], D. Odkhuu[1,3],* N. Tsogbadrakh[3],† and S. C. Hong[2]

[1]*Department of Physics, Incheon National University, Incheon 22012, Republic of Korea*

[2]*Department of Physics and EHSRC,*

University of Ulsan, Ulsan 680-749, Republic of Korea

[3]*Department of Physics, National University of Mongolia, Ulaanbaatar – 14201, Mongolia*

Controlling magnetism of transition metal atoms by pairing with π electronic states of graphene is intriguing. Herein, through first – principle computation we explore the possibility of switching magnetization by forming the tetrahedral sp^3 - metallic d hybrid bonds. Graphene multilayers capped by single – layer cobalt atoms can transform into the sp^3 – bonded diamond films upon the hydrogenation of the bottom surface. While the conversion is favored by hybridization between the sp^3 dangling bonds and metallic d_{z^2} states, such a strong hybridization can lead to the reorientation of magnetization easy axis of cobalt adatoms in plane to perpendicular. The further investigations identify that this anisotropic magnetization even can be modulated upon the change in charge carrier density, suggesting the possibility of an electric – field control of magnetization reorientation. These results provide a novel alternative that would represent tailoring magnetism by means of degree of the interlayer hybrid bonds in the layered materials.

I. INTRODUCTION

The modern field of material science has centered on unique properties of one – to – few atom thick two – dimensional (2D) materials. A prototypical example of one – atom thick 2D system that exhibits a various of fascinating phenomena is graphene [1, 2]. In particular, the engineering of the chemical and physical properties of graphene by decorating with functional or metallic atoms is the most intriguing [3, 4]. Conversely, the presence of graphene substantially alters the electronic and

---

*Electronic address: odkhuu@inu.ac.kr

†Electronic address: Tsogbadrakh@num.edu.mn

magnetic properties of the transition metal atoms, which depends on the degree of hybridization between the metal d orbitals and graphene π bands [5].

Exploring a thermally stable perpendicular magnetization or magnetic anisotropy (PMA) in otherwise nonmagnetic graphene is at the heart of spintronics research. Yet, there have been a few remarkable studies on the magnetic anisotropy of transition metal atoms, mainly cobalt, on graphene [6–9]; for example, unexpectedly large PMA up to an order of 100 meV was predicted in cobalt dimer – benzene pairs [6]. On the other hand, individual Co atoms adsorbed onto graphene on a Pt (111) exhibited an in – plane magnetic anisotropy [10]. Interestingly, subsequent experiments have shown that the preferable magnetization axis of the Co adatoms on graphene is the underlying metal substrate dependence: out – of – plane in Ru (0001) and in – plane magnetization in Ir (111) [7]. The authors attributed this magnetization reorientation to the modified hybridization between the Co($3d$) and graphene p bands by the different graphene/metal interactions (chemisorbed graphene/Ru and physisorbed graphene/Ir and /Pt) [7, 10]. In more recent studies, through C(p_z) - Co(d_{z^2}) hybridization, the presence of fullerene molecules reverses magnetization easy axis of the underlying Co films in plane to perpendicular [8].

In addition to these remarkable findings, the promising alternative for tailoring the ferromagnets anisotropy seemingly resides in the use of even stronger bonding features between the tetrahedral sp^3 and metallic d orbitals [4]. In this article, we propose such argument where the magnetization easy axis of the freestanding Co (0001) monolayer is reversed from in plane to perpendicular by forming the sp^3 - d_{z^2} hybrid bonds, which is driven by the chemical functionalization of the bottom surface of graphene layers. The further investigations identify that this anisotropic magnetization even can be modulated upon the change in charge carrier density, suggesting the possibility of an electric – field control of magnetization reorientation.

II.   METHODOLOGY

Density – functional theory (DFT) calculations were performed using the Vienna *ab initio* simulation package (VASP) [12], and exchange – correlation interactions were described with the generalized gradient approximation (GGA) formulated by Perdew, Burke, and Ernzerhof (PBE) [13]. The modeled structure shown in Fig. 1(b) contains a single layer of cobalt atoms deposited on AB – stacked (Bernal – type

stacking) bilayer graphene, the bottom surface of which is chemically treated with hydrogen atoms. For a reference, the one – side hydrogenated bilayer graphene is illustrated in Fig. 1(a). An energy cutoff of 400 eV and a 21 x 21 x 1 k – mesh were imposed for the lattice and ionic relaxation, where forces acting on atoms were less than 10^{-2} eV/$\overset{\circ}{A}$. Spin – orbit coupling (SOC) term is included using the second – variation method employing the scalar – relativistic eigenfunctions of the valence states [14]. Magnetic anisotropy energy (MAE) is obtained based on the total energy difference when the magnetization directions are in the xy – plane ($E^{\parallel}$) and along the z – axis ($E^{\perp}$), $MAE = E^{\parallel} - E^{\perp}$. A dense k – points of 41 x 41 x 1 was used for MAE calculations, which was sufficient to get reliable results.

III.   RESULTS AND DISCUSSION

We first investigated the structural stabilities of the Co/graphene heterostructure under the bottom surface functionalization. Simulating experimental generation of gas phase atoms of hydrogen that can cover up to half the surface of graphene [15], one of every two atoms of the bottom surface of bilayer graphene is chemisorbed to a hydrogen atom, as shown in Fig. 1(a). The three principle adsorption sites of hydrogen on graphene are taken into account so that to define the most stable atomic structure: namely the hollow, bridge, and top sites. The total energy calculations show that the most stable adsorption site of hydrogen atoms is the top site. After the chemisorption of hydrogen atoms, the two graphene layers can be separated by the van der Waals (vdW) distance or can form interlayer covalent bonds [4]. It has been already indicated in our previous study that the latter structure, i.e., interlayer graphene bonds, is not favored upon the one – side hydrogenation [4]. By contrast, the presence of metal substrate results in the thermodynamically stable sp^3 – bonded carbon films over the metal – free hydrogenated graphene layers [4]. This is also the case for the present system where the other surface of bilayer graphene is covered by the monolayer cobalt atoms (See Fig. 1(b)). Similarly, the two – side hydrogenation (or fluorination) of graphene layers can lead to the favorable C – C interlayer bonds (not shown). Furthermore, we would like to note that the transition barrier from graphene layers to sp^3 – bonded carbon films on metal substrate upon the functionalization was found to be negligibly small [4], which is expected for the present system. It was also reported that no energy barrier is required for the physisorption

– chemisorption transition of the two – side fluorinated BN multilayers [16].

Figure 2 shows the formation energies (H_f), defined as presented in Ref. [4], of the one – side hydrogenated graphene layers with (filled) and without metal adatoms (unfilled symbol) relative to the pristine bilayer graphene. We also present the H_f of the Co adatoms deposited on the pristine bilayer graphene before hydrogenation in Fig. 2. The results indicate an importance of the presence of metal adatoms in the interlayer formation. We therefore attribute the C – C and C – Co chemical bonds to the saturation of the otherwise unstable sp^3 dangling bonds with metal surface states. The driving force for this is the hybridization between the C(sp^3) and Co(d_{z^2}) orbitals at the strong chemical Co – C bonds [4, 11]. Furthermore, such sp^3 – bonded diamond – like carbon structure with metal and functional atoms is estimated to be thermodynamically and structurally stable for the thicknesses of up to eight carbon layers, analogues to that in the functionalized graphene on metal substrate [4]. Similar results were also found for the two – side fluorinated sp^3 – bonded BN multilayers [16].

To better appreciate the strong sp^3 - d_{z^2} hybridization, we plot the electronic band structure and density of states (DOS) of the bonded C and Co atoms in Figs. 3(a,b) and 3(c,d) for the physisorbed and chemisorbed Co/graphene, respectively. The electronic features of the pristine Co and graphene layers remain almost unchanged in the physisorption: the majority (minority) spin states of the ferromagnetic atoms are nearly (partially) filled (unfilled), and a band crossing with Dirac cone shape at the Fermi level of graphene (not shown). On the other hand, as seen in Fig. 3, the feature of common peak structures between the Co(d_{z^2}) and C(p_z) states is apparent throughout the energy level in the chemisorption configuration, indicating the strong orbital hybridization therein. In particular, the existence of these bands in the majority spin state right at the Fermi level is prominent. Such metal –induced gap states (MIGS) can penetrate into up to several – layer thicknesses of graphene, but the C – site induced magnetism (0.08 μ_B) is confined only to the interface layer.

Figure 4(a) shows the calculated MAE of the physisorbed and chemisorbed Co/graphene. The MAE changes its sign from negative (– 0.62 meV) to positive (0.78 meV) at the physisorption – chemisorption (or $sp^2 - sp^3$) transition, which are also well reproduced for the thicker graphene layers. The former and latter stand for the preferable direction of magnetization parallel and normal to the film plane, i.e., PMA. This indicates that the magnetization easy axis of the Co adatoms can be

switched and undergoes a transition from an in – plane to perpendicular magnetiza-
tion upon the formation of $C(sp^3) - Co(d)$ hybrid bonds, as schematically illustrated
in the inset of Fig. 4(a). We further inspect the relationship between the orbital
moment mo and MAE according to Brunos model [17]:

$$MAE = -\frac{\zeta}{4\mu_B}\Delta m_0 \qquad (1)$$

where ζ is the strength of SOC and $\Delta m_0 = m_0^{\parallel} - m_0^{\perp}$. The calculated Δm_0 of the Co
adatoms physisorbed and chemisorbed on graphene are shown at the bottom in Fig.
4(a), where $\Delta m_0 < 0$ and $\Delta m_0 > 0$, respectively. These results adequately obey the
Bruno relation: the easy magnetization axis coincides with the direction that has the
largest orbital moment.

The $sp^2 - sp^3$ transition evolves in different energy landscapes around the Fermi
level, which consequently modulates the MAE. To convince this argument, we follow
the recipe of the second – order perturbation theory by Wang *et al.* [18]: MAE is
determined by the SOC between occupied and unoccupied bands as

$$MAE = \zeta^2 \sum_{o,u} \frac{|<\Psi_o|L_z|\Psi_u>|^2 - |<\Psi_o|L_x|\Psi_u>|^2}{E_u - E_o} \qquad (2)$$

where Ψ_o (Ψ_u) and E_o (E_u) represent eigenstates and eigenvalues of occupied (un-
occupied) states, respectively. Relative contributions of the nonzero and matrix ele-
ments are $<\Psi_{xz}|L_z|\Psi_{yz}>= 1$, $<\Psi_{xy}|L_z|\Psi_{x^2-y^2}>= 2$, $<\Psi_{z^2}|L_x|\Psi_{xz/yz}>= \sqrt{3}$,
$<\Psi_{xy}|L_x|\Psi_{xz/yz}>= 1$ and $<\Psi_{x^2-y^2}|L_x|\Psi_{xz/yz}>= 1$, where the positive and neg-
ative contributions to MAE are characterized by L_z and L_x operators, respectively
[18].

In Fig. 4(b), we assign the energy difference of the largest and closest PDOS peaks
to the Fermi level in the most relevant orbital states, $d_{xz/yz}$ and d_{z^2}, as $E_u - E_o$.
The energetics and MIGS were mainly attributed to the p_z - d_{z^2} hybridization in the
majority spin state, as addressed in Fig. 3. However, from energy – and k – resolved
band analyses, no appreciable coupling of the spin – up occupied and unoccupied d
– orbital states appears near the Fermi level. This is in line with the previous full
– potential studies on a series of $3d$ – to – $5d$ systems [19, 20], in which the spin
channel decomposition terms of MAE that involve the spin – up (↑) state, MAE(↑ ↑)
and MAE(↑ ↓), were not significant. For the Co adatoms physisorbed on graphene,

there are two strong SOC states between the d_{z^2} and $d_{xz/yz}$ orbitals in the minority – spin state, which leads to the negative MAE through $< \Psi_{z^2}|L_x|\Psi_{xz/yz} >$, where $E_{z^2} - E_{xz/yz} = 0.52$ and 1.35 eV. When the sp^2 transforms to the sp^3 phase, the $C(sp^3)$ - $Co(d)$ hybridization splits these minority – spin d_{z^2} states into the low – energy occupied peak at - 2.3 eV and high – energy unoccupied peak at 1.6 eV. Thus, the negative contributions to MAE decrease; instead, the positive contribution through $< \Psi_{xz}|L_z|\Psi_{yz} >$ with $E_{xz} - E_{yz} = 0.91$ eV becomes more dominant. From the k – resolved MAE and spin – down band analyses, these SOC pairs that involve the $d_{xz/yz}$ and d_{z^2} bands are predominant around the K – M line points, at which the dominant contributions of the MAE are also prominent.

The engineering of the MAE by Fermi level shifts further suggests exploring a crucial effect of the external gating on magnetization reorientation. To anticipate this phenomenon, we analyze the Δm_0 of the chemisorbed Co/graphene as a function of excess electron per atom, which reflects to the externally injected charge carrier in a positive gating, in Fig. 5(a). Remarkable, the Δm_0 changes its sign from positive to negative at about 0.1 e/atom. This is due to the nearly flat d_{z^2} band that appears around 0.5 eV above the Fermi level at the K – M points, while the degenerate $d_{xz/yz}$ orbital states become filled. Thereby, the SOC pairs between these filled $d_{xz/yz}$ and empty d_{z^2} bands are formed at the K – M, which should provide the negative MAE(k) therein, as for the case of the physisorption but with the level reversal. As expected, we find that the total MAE changes its sign from the PMA to an in – plane magnetization at around 0.3 e/atom, as seen in Fig. 5(b). These results are of considerable interest in the area of electrically controlled magnetism and magnetoelectric phenomena [21–23].

IV.   CONCLUSION

To summarize, our first – principles computation shows that the magnetization easy axis of the monolayer Co (0001) can reorient from in – plane to perpendicular, when the one – side hydrogenated graphene layers are introduced, by forming the sp^3 - d_{z^2} hybrid bonds. The chemical functionalization of the bottom surface of graphene layers leads the transformation into thermodynamically stable sp^3 – bonded diamond carbon films, which in turn can develop the strong chemical tetrahedral sp^3 – metallic d bonds. Moreover, it is found that the perpendicular spin orientation of the Co

adatoms chemisorbed onto the sp^3 – bonded diamond layers is switchable by altering the density of charge carriers through the application of gate voltage. We thus expect that the present study would provide another novel alternative that would represent tailoring magnetism by means of degree of the interlayer hybrid bonds in the layered materials.

Acknowledgments

[1] K. S. Novoselov, A. K. Geim, S. V. Morozov, D. Jiang, Y. Zhang, S. V. Dubonos, I. V. Grigorieva, and A. A. Firsov, Science **306**, 666 (2004).

[2] X. Li, W. Cai, J. An, S. Kim, J. Nah, D. Yang, R. Piner, A. Velamakanni, I. Jung, E. Tutuc, et al., Science **324**, 1312 (2009).

[3] G. Giovannetti, P. A. Khomyakov, G. Brocks, V. M. Karpan, J. van den Brink, and P. J. Kelly, Phys. Rev. Lett. **101**, 026803 (2008).

[4] D. Odkhuu, D. Shin, R. S. Ruoff, and N. Park, Sci. Rep. **3**, 3276 (2013).

[5] A. V. Krasheninnikov, P. O. Lehtinen, A. S. Foster, P. Pyykko, and R. M. Nieminen, Phys. Rev. Lett. **102**, 126807 (2009).

[6] R. Xiao, D. Fritsch, M. D. Kuzmin, K. Koepernik, H. Eschrig, M. Richter, K. Vietze, and G. Seifert, Phys. Rev. Lett. **103**, 187201 (2009).

[7] F. Donati, L. Gragnaniello, A. Cavallin, F. D. Natterer, Q. Dubout, M. Pivetta, F. Patthey, J. Dreiser, C. Piamonteze, S. Rusponi, et al., Phys. Rev. Lett. **113**, 177201 (2014).

[8] K. Bairagi, A. Bellec, V. Repain, C. Chacon, Y. Girard, Y. Garreau, J. Lagoute, S. Rousset, R. Breitwieser, Y.-C. Hu, et al., Phys. Rev. Lett. **114**, 247203 (2015).

[9] H. Yang, A. D. Vu, A. Hallal, N. Rougemaille, J. Coraux, G. Chen, A. K. Schmid, and M. Chshiev, Nano Lett. **16**, 145 (2016).

[10] F. Donati, Q. Dubout, G. Aut'es, F. Patthey, F. Calleja, P. Gambardella, O. V. Yazyev, and H. Brune, Phys. Rev. Lett. **111**, 236801 (2013).

[11] S. Rajasekaran, F. Abild – Pedersen, H. Ogasawara, A. Nilsson, and S. Kaya, Phys. Rev. Lett. **111**, 085503 (2013).

[12] G. Kresse and J. Hafner, Phys. Rev. B **47**, 558 (1993).

[13] J. Perdew, K. Burke, and M. Ernzerhof, Phys. Rev. Lett. **77**, 3865 (1996).

[14] D. D. Koelling and B. N. Harmon, J. Phys. C Solid State **10**, 3107 (1977).

[15] Z. Q. Luo and et al., ACS Nano **3**, 1781 (2009).

[16] Z. Zhang, X. C. Zeng, and W. Guo, J. Amer. Chem. Soc. **133**, 14831 (2011).

[17] P. Bruno, Phys. Rev. B **39**, 865 (1989).

[18] D. S. Wang, R. Wu, and A. J. Freeman, Phys. Rev. B **47**, 14932 (1993).

[19] D. Odkhuu, S. H. Rhim, N. Park, K. Nakamura, and S. C. Hong, Phys. Rev. B **91**, 014437 (2015).

[20] D. Odkhuu, S. H. Rhim, N. Park, and S. Hong, Phys. Rev. B **88**, 184405 (2013).

[21] W. Eerenstein, N. D. Mathur, and J. F. Scott, Nat. Mater. **442**, 759 (2006).

[22] J. T. Heron, M. Trassin, K. Ashraf, M. Gajek, Q. He, S. Y. Yang, D. E. Nikonov, Y.-H. Chu, S. Salahuddin, and R. Ramesh, Phys. Rev. Lett. **107**, 217202 (2011).

[23] W.-G. Wang, M. Li, S. Hageman, and C. L. Chien, Nat. Mater. **11**, 64 (2012).
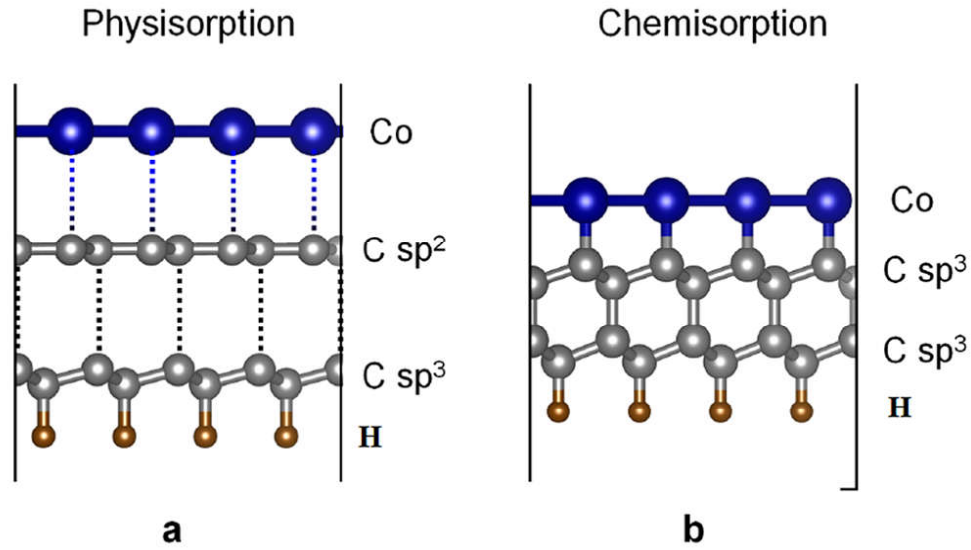
FIG. 1: (Color online) Side views of the optimized atomic structures for the one – side hydrogenated double layer graphene (a) without and (b) with monoatomic – thick Co adatoms on the other side of graphene surface. The hydrogenation of the outer surface of graphene layers induces the interlayer bonding between the graphene layers. The gray, brown, and blue spheres indicate the C, H, and Co atoms, respectively.
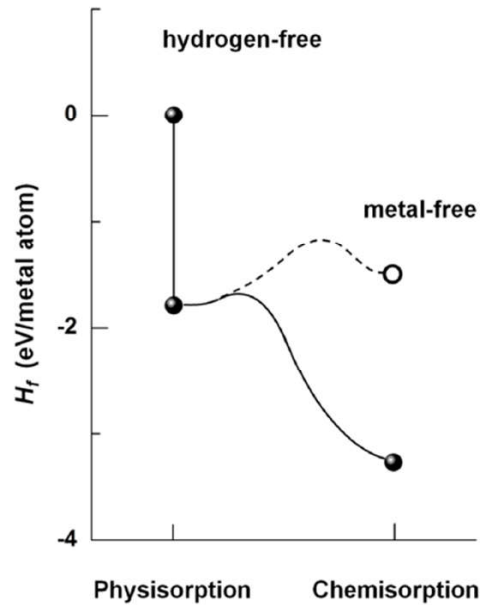

FIG. 2: The formation energy H_f of the physisorbed and chemisorbed Co/graphene (filled circles). The corresponding result for the chemisorbed bilayer graphene without Co adatoms is shown in open circle (metal – free). Total energy of the Co adatoms on bilayer graphene before functionalization is taken as reference energy (hydrogen – free).
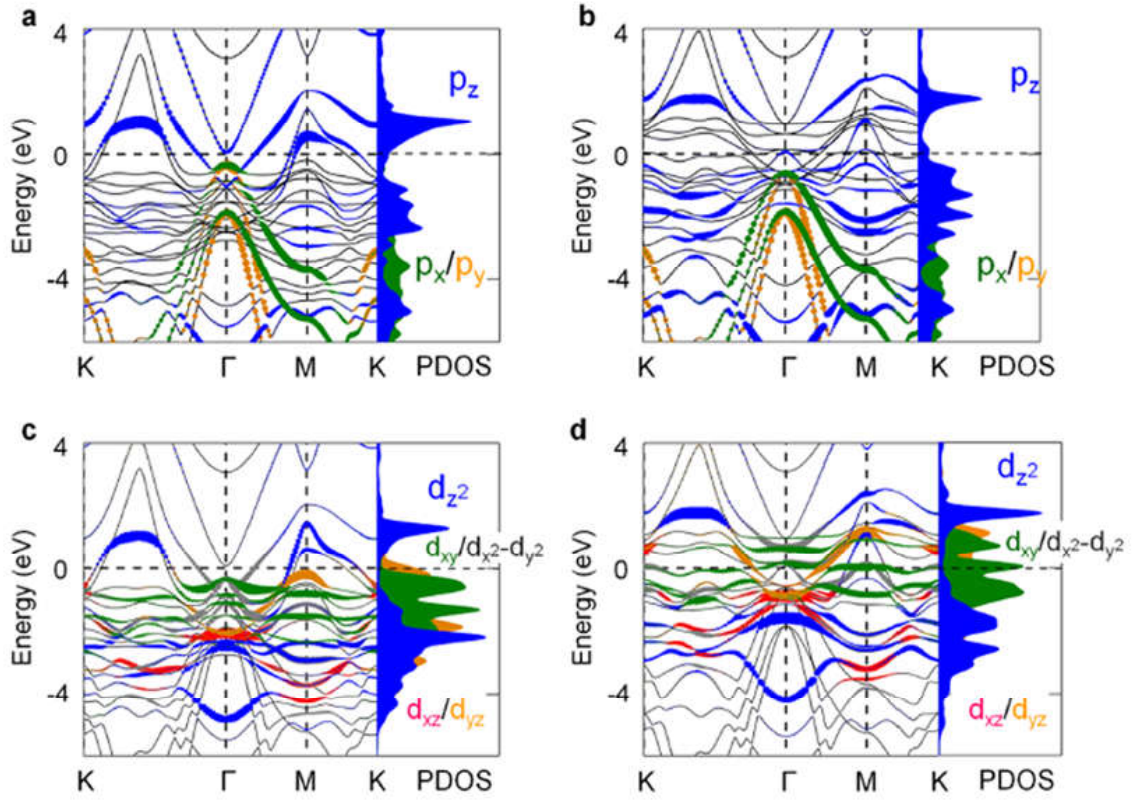
FIG. 3: (Color online) (a) and (c) Spin – up and (b) and (d) spin – down band structures and density of states of the bonded C and Co atoms of the hydrogenated sp^3 graphene layers with Co coverage, respectively. In (a) and (b), the symbols superimposed over the band lines with green, orange, and blue colors represent black, orange, green, red, and blue colors represent the p_x, p_y, and p_z states of the C atom. In (c) and (d), the green, red, orange, blue and black denote the d_{xy}, d_{xz}, d_{yz}, d_{z^2} and $d_{x^2-y^2}$ orbitals of the Co adatom. The size of the symbols is proportional to their weights and the Fermi level is set to zero energy.

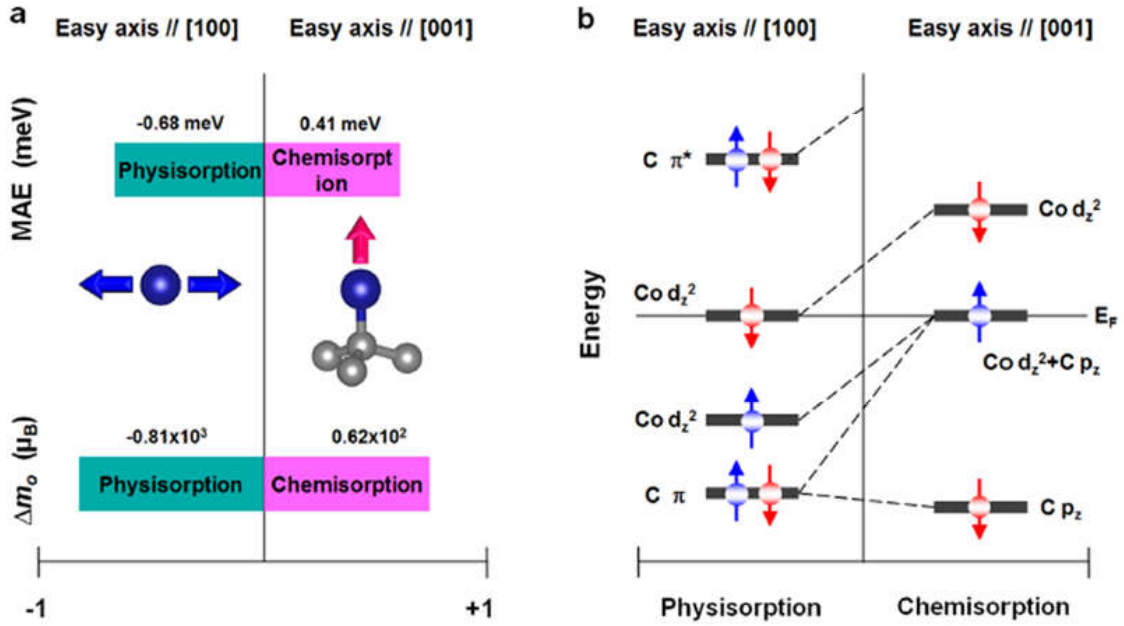FIG. 4: (Color online) (a) MAE (upper) and Δm_0 (lower) of the pristine Co monolayer and Co adatom chemisorbed on the hydrogenated bilayer grahene. (b) Schematic diagram of the single – electron levels of the Co adatom chemisorbed on the hydrogenated bilayer graphene.
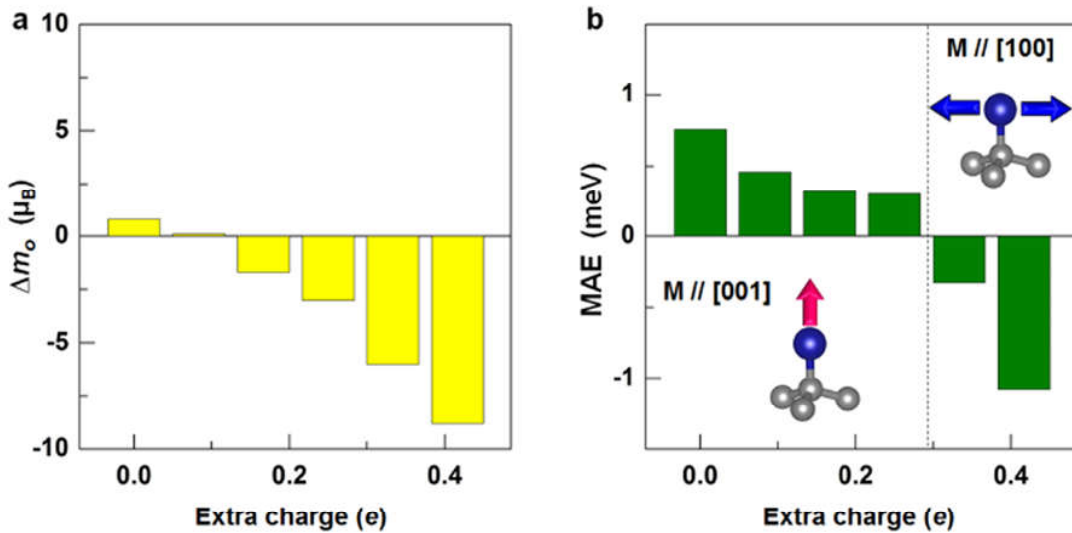

FIG. 5: (Color online) (a) Δm_0 and (b) MAE versus the external electron injection of the Co adatom chemisorbed on the hydrogenated bilayer graphene.

Results of programming static meson system in SU(3) lattice gauge theory

Ch. Sodbileg[1], P. Battogtokh[1], G. Enkhtuya[1]

[1]*Institute of Physics and Technology,*

MAS, Ulaanbaatar 13330, MONGOLIA

Using Monte-Carlo techniques, we have implemented a program that simulates static meson system in SU(3) lattice gauge theory. As a check of the correctness of the program we simulated measurements using our program and then computed some observables which are narrowly defined before in similar works. In this work we have presented expectation value of the plaquette, 2×1 Wilson loops and Polyakov loops as a function of inverse temperature besides the published values of these observables. The comparisons between the observables and its published values are shown that our program works properly.

I. INTRODUCTION

The Monte-Carlo simulation of pure lattice gauge theories are currently playing an important role in the study of confinement and the understanding its dynamics. In particular, four dimensional SU(3) lattice gauge theory[1],[2] is suitable tool for the problems of the strong interaction, because of the strong interactions are described by QCD, and SU(3) gauge theory. Nevertheless many research works such as ref. [4] and [3] that studied the problems of the strong interactions, were simulating in the SU(2) lattice gauge theory. The similarity of SU(3) vacuum structure with the one of SU(2) and also in order to simplify the simulation researchers had been using quenched approximation of SU(2) pure gauge theories without matter field.

Our previous program were simulating the flux tube between a quark and an antiquark at the high temperature in the simpler SU(2) gauge theory[5],[6]. This pure SU(2) gauge theory contains already essential features of flux tube of the $q\bar{q}$ system, but its much simpler than SU(3), and takes much less computational time for the simulation. So in this program we considered pure SU(2) gauge theory which correspond to the case of static quark sources. Nowadays, we need to convert our program into SU(3) lattice gauge theory in order to investigate confinement and strong interactions more narrowly.

In this work we have converted and improved our previous SU(2) program into more accurate program that is based on SU(3) lattice gauge theory. It is reasonable to improve our data sample and hence make a more accurate determination of the flux tube of the $q\bar{q}$ system. And it is the beginning of many further studies such as flux tube of the baryon like systems, a glue ball and asymptotic freedom.

After this part we will assume some lattice observables that are computed by our SU(3) program. In the program we works in a four dimensional lattice in the SU(3) lattice gauge theory. There is a link variable that connect the nearest neibours i and j on the lattice. The link variable is 3×3 unitary unimodular matrices U_{ij} of the group $SU(3)$, with the condition that $U_{ij} = (U_{ji})^{-1}$. We define the partition function on the lattice by

$$Z(\beta) = \int \left(\prod_{ij} dU_{ij} \right) exp(-\beta \sum_{\square} \left(1 - \frac{1}{N_c} ReTrU_{\square} \right)), \tag{1}$$

where β is the inverse temperature given by $\beta = 2N_c/g_0^2$ with g_0 is bare coupling constant and N_c is the number of color, $N_c = 3$. The action defined by $U_{\square} = U_{ij}U_{jk}U_{kl}U_{li}$, which is the product of four link variables around the plaquette. From the eq. (1), expectation value of plaquette is given by

$$P_{\square} = \frac{1}{N_c} ReTrU_{\square}. \tag{2}$$

When an arbitrarily μ by ν closed rectangular contour is denoted by C and U_C is the product of link variables around C, the expectation value of any Wilson loops will be defined via

$$W_{\mu\nu} = \frac{1}{N_c} ReTrU_C. \tag{3}$$

In order to reduce computational time we restricted the program, one can compute plaquette and 2×1 Wilson loops that is defined by the 1 by 2 closed link closed rectangular counter. For the study of $q\bar{q}$ system, Wilson loops no longer play the key role. It will be replaced by Polyakov loops which are gauge invariant quantity

$$L(\vec{n}) = \frac{1}{N_c} Tr \prod_{\tau=1}^{N_\tau} U_4(\vec{n}, \tau). \tag{4}$$

This expression is invariant under periodic gauge transformations. Physical value of the Polyakov loops have a simple physical interpretation that is the free energy of static $q\bar{q}$ pair, one is denoted by $F_{q\bar{q}}(\vec{n}, \vec{m})$. It can be obtained from the correlation

function of two such loops with the base at $\overrightarrow{n}$ and $\overrightarrow{m}$, having opposite orientations that $\Gamma(\overrightarrow{n}, \overrightarrow{m}) = < L(\overrightarrow{n})L^\dagger(\overrightarrow{m}) >$. Time propagation of the two static quarks sitting in the ends of the flux tube are represented by Polyakov loops $L(0)$ and its conjugate $L^\dagger(R)$, which are located a distance R from each other on the lattice. Flux tube profiles can thus be extracted from the correlation of a plaquette with the Polyakov loops

$$f_{\mu\nu}(n_\parallel, n_\perp) = \frac{\beta}{a^4} \left[\frac{< L(0)L^\dagger(R)P_{\mu\nu}(n_\perp) >}{< L(0)L^\dagger(R) >} \right], \tag{5}$$

by varying the distance $n_\perp$ and the orientation of the plaquette with respect to the Polyakov loops. Six different $f_{\mu\nu}$ combinations such as $f_{23} = 1/2(-B_\parallel^2)$, $f_{13} = 1/2(-B_\perp^2)$, $f_{12} = 1/2(-B_\perp^2)$, $f_{14} = 1/2(E_\parallel^2)$, $f_{34} = 1/2(E_\perp^2)$, $f_{24} = 1/2(E_\perp^2)$, define the six components of electric and magnetic field.

In this work we have presented expectation values of plaquette, Wilson loops and Polyakov loop, because of these observables defined most basic baselines. Other observables which are interrupted physical quantities, are shown in further works.

II. THE PROGRAM AND ITS ALGORITHM

We changed our previous SU(2) program into more accurate program that is based on SU(3) lattice gauge theory. Firstly, we have changed mathematical operations such as a addition, subtraction, multiplication, division that are defined between 2×2 matrices, real numbers and complex numbers into operations between the 3×3 matrices and the numbers. In the figure II example of the changed operation shown. This figure shows the C^{++} code of multiplication of two matrices for gauge group of the SU(2) and SU(3). Other codes are presented in appendix. Secondly, we converted

FIG. 1: The C^{++} codes of multiplication of two matrices. **Left** figure is a code of multiplication between two 2×2 matrices and **right** figure is a code of multiplication between two 3×3 matrices

the codes that are generated and unitarized 2×2 matrices and found determinat and trace of the 2×2 matrices, into the code for 3×3 matrices. These codes are shown in the appendix. End of all this work we changed a Monte-Carlo updates from the overrelaxed heatbath algorithm[7] that is used in the previous code into the overrelaxed Metropolis[1]. In Monte-Carlo simulations one has to generate SU(3) matrices with the Boltzmann weight given by eq.(1). Therefore we considered the Metropolis algorithm ref. [10] for the SU(3) program. Schematically the algorithm proceeds as follows:

1. Randomize an input U.

2. **Iterate until** equilibrium is attained.

3.   Generate U^* by performing a random trial move from U

4.   Compute transition probability $Pr(U \to U^*) = min\{1, \frac{Pr(U^*)}{Pr(U)}\}$.

5.   If: $random(0,1] < Pr(U \to U^*)$ then $U \to U^*$.

After the Metropolis we used four overrelaxation steps in ref. [11] to obtain a new gauge configurations. For the overrelaxation algorithm we change nothing and used in our previous work. Finally the SU(3) program became 14 C^{++} header files and these includes 3400.

The simple algorithm is shown in the figure 2. This figure shows the processes that initialize and thermalize link variables and compute the expectation values of the plaquette eq.(2), 2×1 Wilson loops eq.(3), Polyakov loops eq.(4) and polyakov loops - plaquette correlation eq.(5) function on the 4 dimensional lattice in the SU(3) lattice gauge theory.

Then the program computes the expectation value of the plaquette, 2×1 Wilson loops, Polyakov loops and their correlation functions and print every data of these quantities. The figure 2 presents some results of the simulation.

After all the work the SU(3) program worked and printed results, showed in figure II. There is the parallel magnetic field strength $1/2(-B_{\parallel}^2)$ and the parallel electric field strength $1/2(E_{\parallel}^2)$ averaged 20000 iteration at the $R = 4a$ and $\beta = 25$. We can see only the shape of the flux tube profile with the two peak which is shown in figure II. Nevertheless it has a same shape with the theory, we need to check the program more narrowly for the ▬numerical value. That's why we are doing this research.
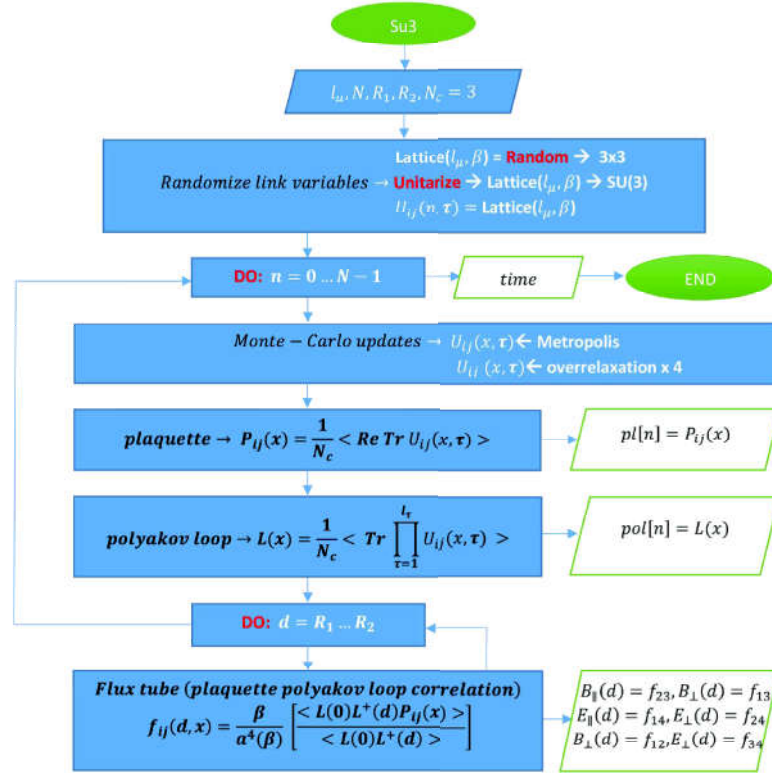
FIG. 2: Schematic structure of the program
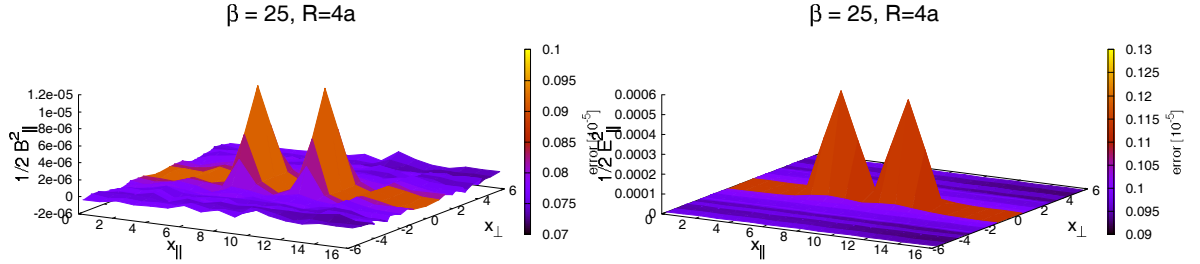
FIG. 3: The parallel magnetic field strength $1/2(-B_\parallel^2)$ a) and the parallel electric field strength $1/2(E_\parallel^2)$ b) at the $R = 4a$ and $\beta = 25$.

III. RESULTS AND COMPARISON

In this work we have presented results that is simulated on lattices of volume 6^4 and 8^4 at 18 values of the β from 1.0 up to 9.5 and compute expectation value of plaquette, 2×1 Wilson loops and Polyakov loops as a function of β. These expectation values have been compared with the similar expectation values which is printed in ref. [8] and [9]. As a check of the correctness of the code, in figure 4 and 5, we compare the

expectation values of the plaquette and 2×1 Wilson loops with the similar values of the ref. [8]. Then we compare expectation value of Polyakov loops with the Polyakov loop of ref. [9].

FIG. 4: Expectation value of plaquette as a function of β on the lattices of volume 6^4 and 8^4.

FIG. 5: Expectation value of 2×1 Wilson loops as a function of inverse temperature from the lattice of volume 6^4.

The figure 4 shows the expectation value of plaquette as a function of β on lattices of volume 6^4 and 8^4. There are three different expectation values of the plaquette which

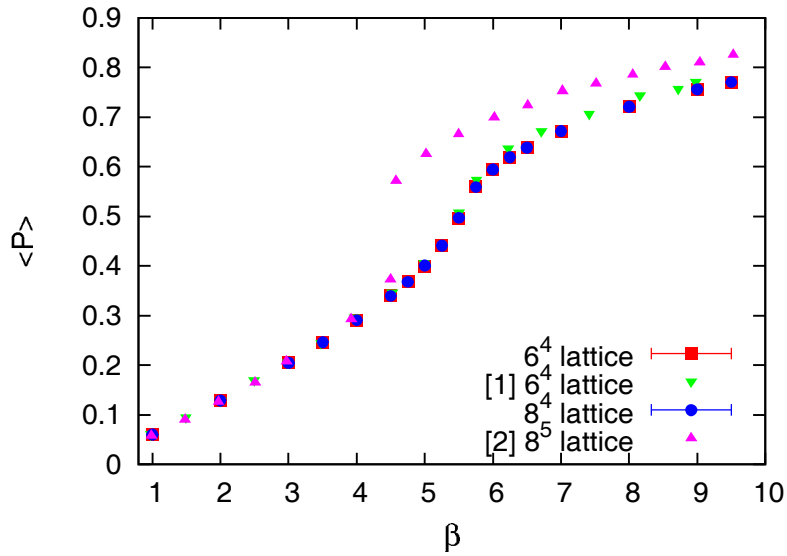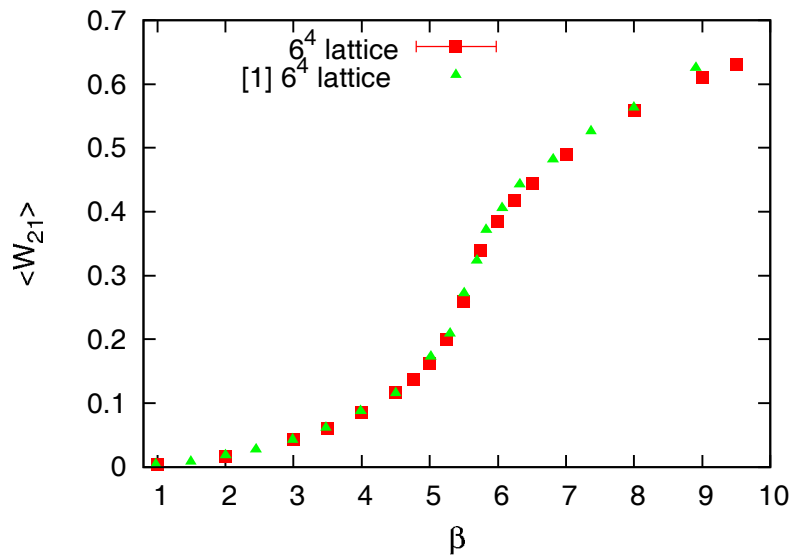are simulated in three individual program. The red square points and the blue circle points denote the expectation value of the plaquette, which simulated our program, respectively on the lattices of volume 6^4 and 8^4. From these two data points we can see that the expectation value of plaquette doesn't depend on lattice size. The plaquette data which are presented in ref. [8] on the lattice of volume 6^4, are denoted by down triangle in the figure 4. These points had a same value with our plaquette value. It shows that our program well defined the lattice field. In the figure 4 the up triangle points denotes the expectation value of the plaquette which are presented in the ref. [9] on the lattice of volume 8^5. These points have a identical value with our plaquette data when $\beta > 4.5$, besides they have a different value with our data points. In the ref. [9] the expectation values are computed in five dimensional lattice, nevertheless our values computed in four dimensional lattice. Thats why the expectation values of plaquette had different each other.

In the figure 5, there are squared red points that denote our Wilson loops value and up triangle green points that denote the expectation value of the 2×1 Wilson loops in ref. [8]. We compare the expectation value of the 2×1 Wilson loops as a function of β which is simulated our program with the expectation value of the Wilson loops as a function of β which is presented in ref. [8]. From the comparison, we can see that there is no difference. This shows our program define lattice properly.
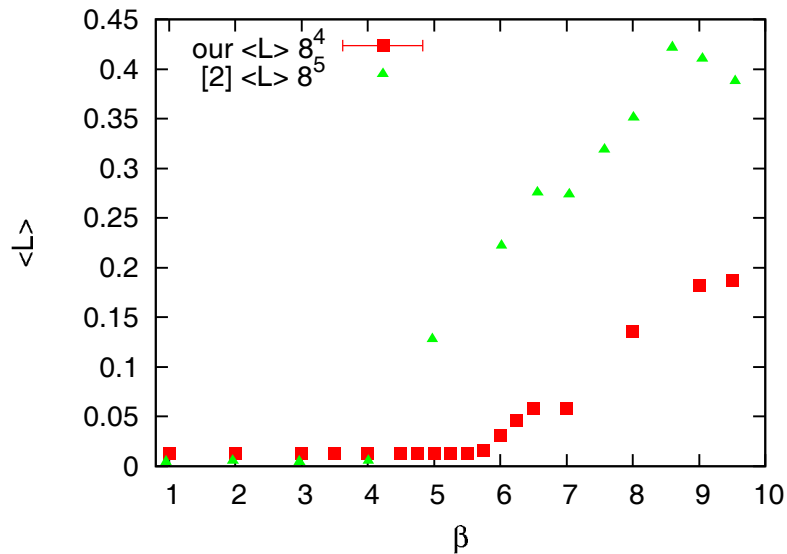

FIG. 6: Expectation value of Polyakov loops as a function of β from the lattice of volume 8^4.

The figure 6 presents the average expectation value of Polyakov loops as a function of β from the lattice of volume 8^4. The down triangle points denote the Polyakov loops which is cited from the ref. [9]. The red squared points presents the value of Polyakov loops which is simulated our program. These squared points has a more smaller value than triangle points. This shows that lattice dimension affects the expectation value of Polyakov loops.

IV.   CONCLUSION

We have changed and improved our previous SU(2) program into more accurate program that is based on SU(3) lattice gauge theory. In this work we have defined the base quantities using this new program according to the initial conditions that are defined in ref. [8] and [9]. Therefore we simulated the program on the lattices of volume 6^4 and 8^4 at the value of β from 1.0 up to 9.5. From these simulation, we computed the expectation value of plaquette, 2×1 Wilson loops and Polyakov loops as function of β. Our expectation values of plaquette and the Wilson loops are almost same values with the expectation values which are presented in the ref. [8]. The expectation values in ref. [9] are simulated in the five dimensional lattice, whereas the expectation values that are presented in the ref. [9] and computed in our program have different numerical values and similar functional dependency on the β. From these comparisons, we conclude that our program works properly.

[1] E. Pietarinen, Nucl. Phys. B190, 349 (1981).

[2] M. Creutz, Phys. Rev. Lett. 45, 313 (1980).

[3] J. Kuti, J. Polonyi and K. Szalachanyi, Phys. Lett. B98, 199 (1980).

[4] M. Cruetz, Phys. Rev. Let. V43 553 (1979).

[5] S. Chagdaa, Doctoral dissertation, (2008).

[6] S. Chagdaa et. al., J. Phys. G. (In review).

[7] S. L. Adler, Phys. Rev. D 23, 2901 (1981).

[8] M. Creutz, Phys. Rev. D. 26 (8) 1982.

[9] E. Itou, et al., Prog. Theor. Exp. Phys. 2012, 0000, 23 (2012).

[10] N. Metropolis et al., J. Chem. Phys. 21, 1087 (1953).

[11] M. Creutz, Phys. Rev. D36, 515 (1987).

V.   APPENDIX

In this appendix we have shown the figures of the codes that are expressed operation between matrices, real and complex numbers. The right hand side figures are in 2×2 besides the right hand side figures are in 3×3.

```
25  su2 operator+(const su2 &x,const su2 &y)
26  {
27      return su2 (x._e11+y._e11,x._e12+y._e12);
28  }
```

```
32  su3 operator+(const su3 &x,const su3 &y)
33  {
34      return su3 (x._e00+y._e00,x._e01+y._e01,x._e02+y._e02,
35              x._e10+y._e10,x._e11+y._e11,x._e12+y._e12,
36              x._e20+y._e20,x._e21+y._e21,x._e22+y._e22);
37  }
```

FIG. 7: The codes of addition between two matrices.

```
28  }
29  su2 operator+(const prec_float &x,const su2 &y)
30  {
31      return su2 (x+y._e11,y._e12);
32  }
```

```
38  su3 operator+(const prec_float &x,const su3 &y)
39  {
40      return su3 (x+y._e00,y._e01,y._e02,
41              y._e10,x+y._e11,y._e12,
42              y._e20,y._e21,x+y._e22);
43  }
```

FIG. 8: The codes of subtraction between matrices and real numbers.

```
50  su2 operator-(const prec_float &x,const su2 &y)
51  {
52      return su2 (x-y._e11,-y._e12);
53  }
```

```
69  su3 operator-(const prec_float &x,const su3 &y)
70  {
71      return su3 (x-y._e00,-y._e01,-y._e02,
72              -y._e10,x-y._e11,-y._e12,
73              -y._e20,-y._e21,x-y._e22);
74  }
```

FIG. 9: The codes of subtraction between the matrices and real numbers.

```
su2 operator*(const prec_complex &x,const su2 &y)
{
    return su2 (x*y._e11,x*y._e12);
}
```

```
93  su3 operator*(const prec_complex &x,const su3 &y)
94  {
95      return su3 (x*y._e00,x*y._e01,x*y._e02,
96              x*y._e10,x*y._e11,x*y._e12,
97              x*y._e20,x*y._e21,x*y._e22);
98  }
```

FIG. 10: The codes of multiplication between the matrices and complex numbers.

```
su2 operator/(const su2 &x, int y)
{
    return su2 (x._e11/static_cast<double>(y),x._e12/static_cast<double>(y));
}
```

```
su3 operator/(const su3 &x, int y)
{
    return su3 (x._e00/static_cast<double>(y),x._e01/static_cast<double>(y),x._e02/static_cast<double>(y),
            x._e10/static_cast<double>(y),x._e11/static_cast<double>(y),x._e12/static_cast<double>(y),
            x._e20/static_cast<double>(y),x._e21/static_cast<double>(y),x._e22/static_cast<double>(y));
}
```

FIG. 11: The codes for matrix divide by numbers.

```
prec_float tr_d(const su2 &x)
{
    return prec_float (2* real(x._e11) );
}
```

```
prec_float tr_d(const su3 &x)
{
    return prec_float (real(x._e00)+real(x._e11)+real(x._e22));
}
```

FIG. 12: The codes for trace

```
prec_float su2::det(const su2 &x)
{
    return(real(x._e11*conj(x._e11) + x._e12*conj(x._e12)));
}
```

```
prec_float su3::det(const su3 &x)
{
    return(real(x._e00*x._e11*x._e22+x._e01*x._e12*x._e20+x._e02*x._e10*x._e21-
        x._e01*x._e11*x._e20-x._e01*x._e10*x._e22-x._e00*x._e12*x._e21));
}
```

FIG. 13: The codes for finding determinant

```
void su2::unitarize()
{
    prec_float res;

    res = real(_e11)*real(_e11) + imag(_e11)*imag(_e11) +
        real(_e12)*real(_e12) + imag(_e12)*imag(_e12);
    res=1.0/sqrt(res);

    _e11=_e11*res;
    _e12=_e12*res;
}
```

```
void su3::unitarize()
{
    prec_float res, res1, res2, res3;

    res1 = real(_e00)*real(_e00) + real(_e10)*real(_e10)+ real(_e20)*real(_e20)
        + imag(_e00)*imag(_e00) + imag(_e10)*imag(_e10)+ imag(_e20)*imag(_e20);
    res2 = real(_e01)*real(_e01) + real(_e11)*real(_e11)+ real(_e21)*real(_e21)
        + imag(_e01)*imag(_e01) + imag(_e11)*imag(_e11)+ imag(_e21)*imag(_e21);
    res3 = real(_e02)*real(_e02) + real(_e12)*real(_e12)+ real(_e22)*real(_e22)
        + imag(_e02)*imag(_e02) + imag(_e12)*imag(_e12)+ imag(_e22)*imag(_e22);

    res=1/sqrt(MAX(res3,MAX(res1,res2)));

    _e00=_e00*res;
    _e01=_e01*res;
    _e02=_e02*res;
    _e10=_e10*res;
    _e11=_e11*res;
    _e12=_e12*res;
    _e20=_e20*res;
    _e21=_e21*res;
    _e22=_e22*res;
}
```

FIG. 14: The codes for untarize

```
su2 tilde(const su2 &x)
{
    su2   tmp;

    tmp._e11 = conj(x._e11);
    tmp._e12 = - x._e12;

    return(tmp);
}
```

```
su3 tilde(const su3 &x)
{
    su3 tmp1, tmp;
    tmp1._e00 = conj(x._e00);
    tmp1._e01 = conj(x._e01);
    tmp1._e02 = conj(x._e02);
    tmp1._e10 = conj(x._e10);
    tmp1._e11 = conj(x._e11);
    tmp1._e12 = conj(x._e12);
    tmp1._e20 = conj(x._e20);
    tmp1._e21 = conj(x._e21);
    tmp1._e22 = conj(x._e22);

    tmp._e00 = tmp1._e00;
    tmp._e01 = tmp1._e10;
    tmp._e02 = tmp1._e20;
    tmp._e10 = tmp1._e01;
    tmp._e11 = tmp1._e11;
    tmp._e12 = tmp1._e21;
    tmp._e20 = tmp1._e02;
    tmp._e21 = tmp1._e12;
    tmp._e22 = tmp1._e22;

    return(tmp);
}
```

FIG. 15: The codes for finding reverse matrices

```
void su3lattice::metropolis_11()
{

  su3    new_link;
  su3    staple;
  int    mu_l;
  prec_float s_old, s_new, s_diff, rnd;
  prec_float diff;
  int    akzi,ind;
  int    site;

  diff = 0.0;
  akzi = 0;

  for(register int mu=0;mu<4;mu++)
    {
      mu_l = mu * _vol4;
      for(register int siteh=0;siteh<_vol4;siteh++)
      {
        site = _even_odd[siteh];
        staple = staple_11(site,mu);
        ind = (int)(NR_GEN * drand48());
        new_link= _lattice[site+mu_l]*_new_gen[ind];

        s_old  = _beta * tr_d ( _lattice[site+mu_l] * staple ) / 3.0 ;
        s_new  = _beta * tr_d ( new_link * staple ) / 3.0 ;
        s_diff = s_old - s_new;
        diff   += s_diff;

        if (s_diff < 0.0)
          {
            _lattice[site+mu_l] = new_link;
            akzi++;
          }
        else
          {
            rnd   = drand48();
            if (rnd<exp(-s_diff))
            {
              _lattice[site+mu_l] = new_link;
              akzi++;
            }

          }
      }
    }
}
```

FIG. 16: Metropolis code for 3×3 lattice gauge theory

The roughening transition at finite temperature

G. Enkhtuya, Ch. Sodbileg, P. Battogtokh

Institute of Physics and Technology,

MAS, Ulaanbaatar 13330, MONGOLIA

In this work, we have intended to observe the roughening transition at finite temperature which occurs at zero temperature in confined phase. We have confirmed that the width of the flux tube increases with $q\bar{q}$ separation and also showed that the width rises steeply when the coupling constant has reached at a certain value.

I. INTRODUCTION

It is important to understand the mechanism of the quark confinement phenomenon for study of Quantum chromodynamics (QCD). Confinement is a phenomenon that for large separation, the potential between the quarks increases linearly with the separation, whereas for short separation, the potential depends on the coupling constant logarithmically, in which Coulomb-like potential dominates as the same as the dipole field of the electrodynamic. The coefficient which is the linearly increasing part of the potential is called that string tension (σ).

The study of QCD at the finite temperature and density is relevant for the heavy-ion collision experiments and for the astrophysical problems. One can see reviews in Refs.[1–4] that as temperature increases, the potential decreases due to the temperature dependent string tension but keeps rising as the $q\bar{q}$ separation increases and that the slope of the potential decreases as the temperature increases.

The linear potential causes on the appearance of flux tube which derived between a quark and an antiquark and is the force between the quarks which are at a certain distance from each other. By numerical simulation, one can measure this force only in case of relatively small value of $q\bar{q}$ separation. Distance between quark and antiquark depends on lattice spacing a and choosing a is very sensitivity and one of the difficult problems. If one chose too large a, it will be difficult to see continuum physics and if a is too small, one cannot expect to see asymptotic form of the force on lattice with small extent.

The static $q\bar{q}$ potential form in lattice unit can in principle be determined by cal-

culating the following limit:

$$V(R) = -\lim_{T\to\infty}\left[\frac{1}{T}\ln W(R,T)\right] \tag{1}$$

where $W(R,T)$ is the expectation value of the Wilson loop with spatial and temporal extension R and T, respectively.

The expectation value of the Wilson loop has behaviour that it determines by area law (σRT) in confined phase while by perimeter law ($\sigma(R+T)$) in deconfined phase. Assuming that $W(R,T)$ has the form

$$W(R,T) = e^{-\sigma RT - \alpha(R+T) + \gamma}. \tag{2}$$

We can isolate the σ by studying the Creutz ratios[5]

$$\chi(R,T) = -\ln\left(\frac{W(R,T)W(R-1,T-1)}{W(R,T-1)W(R-1,T)}\right). \tag{3}$$

In other words, if the Wilson loop depends on R and T in the way given by Eq. 2, then $\chi(R,T)$ will be independent of these variables, and will coincide with the string tension.

To date, value of string tension in physical units is still not yet reliably established and its dependence on other physical quantities has studied by lattice numerical simulation with high precision. In particular, σ is very sensitive for gauge groups and it gives different values for each dimension of gauge groups. The mechanism of quark confinement in both QCD and SU(N) pure gauge theories is rather analogous. The value is $N = 3$ for QCD. Even though, SU(N) pure gauge theory gives us a better way to understand the confinement well. Namely, for $N > 3$, new forms of the flux tube which contains different string tensions have appeared.

Recently, in 2012, Cardoso and Bicudo[6] have extracted the string tensions from color averaged free energy of a quark and an antiquark pair and for different spatial lattice volumes, it showed in Fig. 1. They concluded that for the lattice with small extent, the string tension increases with volume and the influence of volume on the string tension disappeared for larger volume.

Also, they have investigated critical curve of σ as a function of temperature in [6]. They observed that the string tension at $0.5T_c$ is practically equal to the σ_0 at zero temperature and further, the string tension decreased as temperature increased.

During the attempts to determine value of the string tension, a transition observed in which the behaviour of the string tension was changing in confined phase. This
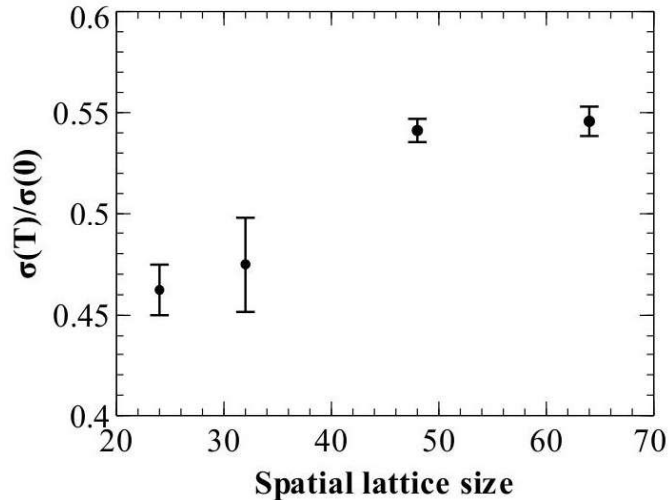
FIG. 1: The string tensions as a function of the spatial lattice size[6].

transition is called that **roughening transition** and this phenomenon is a kind of surface roughening transition. The roughening is well known phenomenon in three dimensional statistical mechanics that explains delocalization between the two phases with enough energy[7]. This phenomenon has investigated for abelian groups $U(1)$ and $Z(N)$ and non-abelian groups $SU(N)$ in three, four and arbitrary dimensions [8–12]. When this transition occurred, the width of the flux tube completely diverges and the surface of the flux tube delocalizes, but the value of the string tension is not zero and still finite near the roughening temperature according to theory of lattice QCD.

This phenomenon is not a transition from confined phase to deconfined phase. Because, if Wilson loop characterized by the area law and the string tension is not zero, then one assume the quark confinement still does.

Since the confinement is directly related to the formation of flux tube, it is necessary to study the relationship of the flux tube and other physical quantities to understand the phenomenon of confinement well.

In this work, our purposes were to study how the width of the flux tube depends on the coupling constant i. e. on the temperature. In other words, does the width of flux tube diverge at finite temperature? What is the value of the coupling constant if it does? At zero temperature, it diverges when $\beta \approx 1.9$. Is the value of coupling constant the same as the one at zero temperature? Or not? We have conducted our research to get answers for these questions.

This article is as follows. Chapter 1 describes fundamental theory, Chapters 2 and 3 describe brief introduction of the strong coupling expansion and the flux tube. It also contains the first main results. In Chapter 4, we present our measurement and the results. Finally, Chapter 5 includes the conclusion.

II.   STRONG COUPLING EXPANSION

Several interesting aspects, like dynamical mass generation, quark confinement etc. are inaccessible to a perturbative treatment and require non-perturbative methods. One of these is the method of strong-coupling expansions, which amount to expansions in powers of the lattice coupling constant (β). Strong-coupling expansions are tied to the lattice and cannot be derived directly for a continuum theory.

In contrast to perturbation theory, which only yields asymptotic expansions, the strong-coupling expansion has a finite range of convergence. Within this range the strong-coupling expansion can be employed by lattice gauge theory to obtain information about quark confinement. Also this method can be used to verify results of Monte Carlo simulation. Strong coupling expansion is well-tested method in describing phase transitions.

As explained in introduction section, the Wilson loop criterion is very important since it allows us to distinguish different phases which with and without quark confinement, by values of gauge invariant observables.

With regard to the analogy between Euclidean quantum field theory in terms of functional integrals and statistical mechanics we have seen that the bare coupling constant squared g^2 plays the role of an analogue temperature. Lattice gauge theory at strong coupling thus corresponds to a statistical system at high temperatures, i.e. small β. Therefore the well-known method of high-temperature cluster expansions of statistical mechanics suggests itself to be applied to this situation.

Behaviour of vortex free energy is analogy to expectation value of Wilson loop which obeys an area law behaviour at zero temperature in confined phase. The coefficient of the area is equal to string tension between the static sources.

Münster has calculated that strong coupling expansion up to order β^{12} from vortex free energy by $SU(2)$ pure lattice gauge theory for four dimension at zero temperature in 1981[13]

$$\sigma_{\infty} = -\ln u - 4u^4 + 8u^6 - 12u^4\nu - 56u^8 + 120u^1 0 - 168u^8\nu -$$
$$- 72u^6\nu^2 - 12\nu^5 - \frac{4732}{3}u^{12} + 888u^{10}\nu - 396u^8\nu^2$$
$$- 48u^6\nu^3 - 48u^4\nu^4 + 36\nu^6 - 48u^9w - 24\nu5wu^{-1}\ldots =$$
$$= -\ln u - 4u^4 - \frac{176}{8}u^8 - \frac{10936}{405}u^{10} - \frac{1532044}{1215}u^{12} - \cdots. \qquad (4)$$

Also, Creutz has obtained values of the string tension by means of the $SU(2)$ theory from Monte Carlo simulation[14]. The two results above together as a function of coupling constant plotted in Fig. 2. The figure also contains exponential curve of weak coupling expansion predicted by renormalization group that expressed in the formula: $\exp\left(-\frac{6\pi}{11}(\beta - 2)\right)$. To compare with the twelfth order result, the lowest order results of the strong coupling expansion also has included in the figure. According to this figure, the MC data follows the exponential curve of the weak coupling expansion in the narrow "window" $2.2 < \beta < 2.5$. In other words, the string tension transforms from the strong coupling behaviour to the weak coupling behaviour. Besides, one can see that the curve of the strong coupling expansion when calculate up to the twelfth order follows the curve of the weak coupling expansion. This is roughening transition. Namely, it proved that the transition occurs when reached at a certain value of β by either theory or results of simulation.
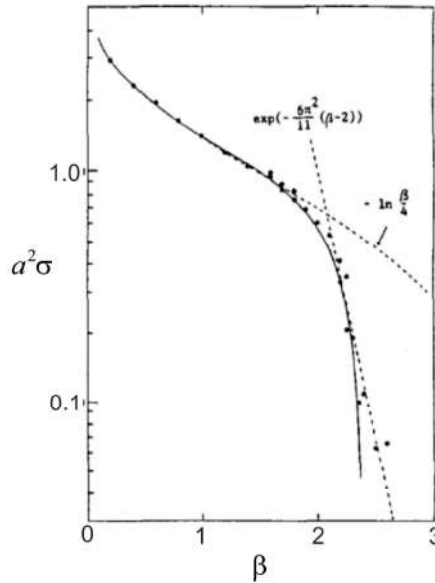

FIG. 2: The string tension as a function of the coupling constant[13].

In 2008, Münster et.al. has calculated the first several order of the strong coupling

expansion for finite N_τ and i.e. at finite temperature[15]

$$f(N_\tau, u) = -\frac{3}{N_\tau} u^{4N_\tau} c^{N_\tau} \left[1 + 12 N_\tau u^4 - \frac{1556}{81} N_\tau u^6 + \right.$$
$$\left. + \left(83 N_\tau^2 + \frac{41417}{243} N_\tau \right) u^8 + O(u^1 0) \right] \tag{5}$$

where $u = \dfrac{I_2(\beta)}{I_1(\beta)} = \dfrac{1}{4}\beta - \dfrac{1}{96}\beta^3 + \dfrac{1}{1536}\beta^5 - \dfrac{1}{23040}\beta^7 + O(\beta^9)$.

It is necessary to compare the results of the strong coupling expansion at finite temperature with results of simulation for further study.

III.   WIDTH OF THE FLUX TUBE

One can also determine signal from a structure and a formation of the flux tube which is string tension is translating from strong coupling regime to weak coupling regime. Therefore, we necessary to assume quantity that the width of the flux tube. We consider transverse profiles of energy density in the tube the physical width of the flux tube. The energy density of the color field can be expressed by[16]

$$\mathcal{E}(x) \propto \langle q\bar{q}|TrE^2(x)|q\bar{q}\rangle - \langle q\bar{q}|q\bar{q}\rangle\langle TrE^2(x)\rangle. \tag{6}$$

When we regularize the theory on lattice this equation becomes:

$$\mathcal{E}(x) \propto \frac{\langle W(C)P_x\rangle - \langle W(C)\rangle\langle P_x\rangle}{\langle W(C)\rangle}. \tag{7}$$

where $W(C)$ is Wilson loop and P_x is plaquatte. At finite temperature, we can consider a pair of Polyakov loops. The lattice operator the becomes:

$$\mathcal{E}(x) \propto \frac{\langle L(0)L(R)P_x\rangle - \langle L(0)L(R)\rangle\langle P_x\rangle}{\langle L(0)L(R)\rangle} \tag{8}$$

where $L(0)$ and $L(R)$ are two Polyakov loops separated by R lattice spacing and again P_x is a plaquette localized in x. Hence, we can calculate the transverse profile of the energy density

$$D^2 = D^2(R/2) = \frac{\int d^2 x_\perp x_\perp^2 \mathcal{E}(x)}{\int d^2 x_\perp \mathcal{E}(x)}. \tag{9}$$

In 1981, Lüscher et. al. has calculated the width of the flux tube up to twelfth order by the method of the strong coupling expansion at zero temperature[16]

$$D_\infty^2 = 4\left\{ u^4 + 2u^6 + \frac{92}{3}u^8 + \frac{37724}{405}u^{10} + \frac{1412551}{1215}u^{12} + \cdots \right\}. \tag{10}$$

They have plotted the expansion as a function of the coupling constant. This figure is shown in Fig. 3. In the figure, σ is rising monotonically, we well-known as the fluctuation of the effective string in confined phase, from zero at $\beta = 0$ to about 0.5 until $\beta = 2$. But, for $\beta \gtrsim 2$, rises steeply. This value coincides with the coupling constant which is string tension extracted from MC simulation carried out by Creutz that is from strong to weak coupling behaviour.
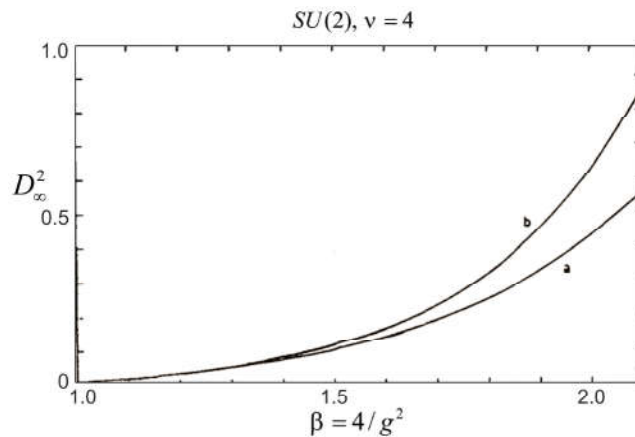

FIG. 3: The width of the flux tube as a function of β[16].

Also in this paper[16], they have assumed that $\sigma \cdot D^2_\infty$ should approach a constant value for $\beta \gtrsim 2$, if $D^2_\infty < \infty$ in the continuum limit. Then they has derived $\sigma \cdot D^2_\infty$ using the strong coupling series that calculated in [13]

$$(\sigma D^2_\infty)^{-1} = \frac{-1}{4u^4 \ln u} \left\{ 1 - 2u^2 - 4u^4 \left(\frac{20}{3} + \frac{1}{\ln u} \right) + 4u^6 \left(\frac{2179}{405} + \frac{2}{\ln u} \right) \right.$$
$$\left. - u^8 \left(\frac{244903}{1215} - \frac{48}{\ln u} - \frac{16}{(\ln u)^2} \right) + \cdots \right\}. \tag{11}$$

The corresponding 6th (a) and 8th (b) order curves are shown in Fig. 4. Rather than approaching a constant, $(\sigma D^2_\infty)^{-1}$ seems to vanish at about $\beta \simeq 1.9$. This value is just below the crossover region $\beta \gtrsim 2$. Here, one assumes D^2_∞ is diverges and this value of the coupling constant named roughening value (β_R). At the roughening point the width of the flux tube is completely delocalized, but it has a finite intrinsic width and tension.

Our purposes were to determine the width of the flux tube by processing our simulation data and to observe its dependence on the interquark distance and on the coupling constant. We fitted a coulombic[17]
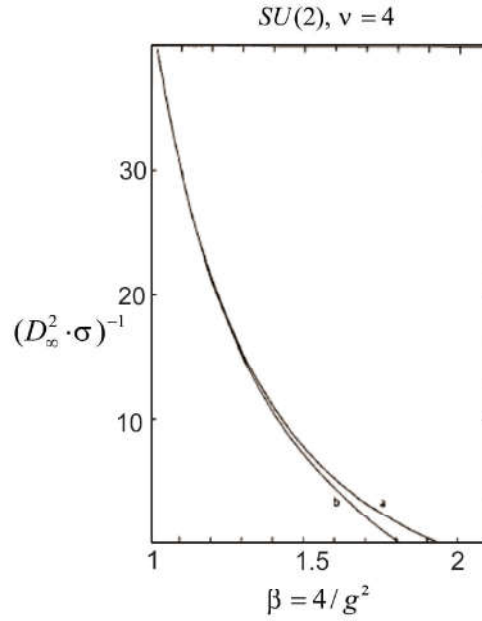
$$\frac{a_1}{(a_2 + x^2_\perp)^3} \tag{12}$$

FIG. 4: $(\sigma D_\infty^2)^{-1}$ versus β. a and b denote 6th and 8th order curves respectively[16].

and an exponential

$$b_1 e^{-b_2 x_\perp} \tag{13}$$

fit functions to the transverse profiles of chromoelectric and chromomagnetic fields results and then calculated the width of the flux tube by the integration of Eq. 9 using the fit parameters. The all components of the chromomagnetic field and the perpendicular component of the chromoelectric field are approximately equal, but the parallel component of chromoelectric is higher than the others[3]. Therefore, we fitted only to the parallel components of the electric and magnetic fields. In our case, the distribution of magnetic field is closely described by the coulombic fit functions, while for the electric field, it needs an addition exponential function. We found that the fit functions

$$\frac{1}{2\beta} B_\parallel^2(r, x_\perp) = \frac{a_1}{(a_2 + x_\perp^2)^3}, \tag{14}$$

$$\frac{1}{2\beta} E_\parallel^2(r, x_\perp) = \frac{a_1}{(a_2 + x_\perp^2)^3} + b_1 e^{-b_2 x_\perp} \tag{15}$$

describe our data better. The physical width of the flux tube is given by

$$a^{-2} D^2 = \frac{6}{(b_2)^2} \tag{16}$$

in terms of the fit parameters.

IV.   MEASUREMENTS AND RESULTS

The simulations performed on lattice of size $16 \times 8^2 \times 4$ and the distance between the quark and the antiquark were $4a - 8a$. For $N_\tau = 4$, the critical value of coupling constant is $\beta_c = 2.2985 \pm 0.00006$ which is phase transition from the confined to the deconfined phase and in order to observe roughening phenomenon we should perform measurement in confined phase. Also, we have to compare our results with the coupling constant which is value of the roughening transition at zero temperature. To meet the two criteria and to do our simulation, we chose $\beta = 1.6$, 1.7, 1.8, 1.9, 2.0, 2.1, 2.2, for the values of the coupling constant. The number of the measurements was 400000 and we processed data.

TABLE I: Results for the fit parameters and the width of the flux tube $(a^{-2}D^2)$

r/a	β	a_1	a_2	b_1	b_2	$a^{-2}D^2$	χ^2
4	1.6	8.36(15.25)	2.55(1.79)	-0.56(31)	0.87(44)	7.92(37)	0.154
	1.7	3.49(14.00)	0.94(1.19)	3.19(3.44)	1.35(69)	3.24(94)	0.0034
	1.8	-616.14(4.90)	24585.9(6.5E+16)	-2.70(3.29)	2.56(1.36)	0.91(22.12)	0.0092
	1.9	9708.2(2.09E+04)	77.80(60.36)	0.23(02)	3.72(1.73)	0.35(6.12)	0.0062
	2.0	-5136(9227)	66.98(43.47)	0.13(1)	0.95(9)	6.64(2.27)	0.6075
	2.1	1.52(42)	4.55(52)	0.053(1)	1.29(5)	3.61(93)	0.2695
	2.2	0.57(14)	2.93(26)	0.0100(6)	0.65(4)	14.20(1.47)	5.17
6	1.6	2.45E-05	0.09(62.93)	-0.09(4)	-0.04(16)	3750(96)	0.02656
	1.7	-9.05E+05	316.59(1737.00)	0.17(7)	0.097(17)	740.74(45.34)	0.0534
	1.8	10138.7(1.504E+04)	37.62(21.1)	-0.21(8)	0.17(14)	207.61(19.76)	0.0942
	1.9	3.39(14.28)	0.94(1.26)	-3.24(2.83)	1.23(16)	3.96(3.12)	0.0515
	2.0	0.008(2)	-0.47(7)	0.22(34)	0.76(8)	10.38(2.52)	0.3165
	2.1	165(430)	26.66(26.39)	0.02(1)	1.97(1.89)	1.54(23.02)	0.2059
	2.2	0.43(82)	4.90(3.39)	0.010(2)	0.62(15)	15.60(5.80)	1.36
8	1.6	2.54E+07(3.58E+08)	646(3041)	0.20(4)	0.02(8)	15000(96)	0.0684
	1.7	-1.68(4.67)	2.38(2.36)	0.01(10)	1.22(9.73)	4.03(191.41)	0.0991
	1.8	18.54(29.09)	5.23(54.32)	0.33(7)	0.33(9)	0.55(6.54)	0.0754
	1.9	-189864(1.52E+06)	202.02(560.9)	0.06(1)	0.04(10)	113.42(2.08)	0.0514
	2.0	-65.46(165.7)	12.05(11.31)	0.029(21)	-0.10(23)	600(55.2)	0.0842
	2.1	-6.51E+06(4.44E+07)	560(1224)	0.050(9)	0.10(7)	495(15.27)	0.1238
	2.2	0.22(30)	3.73(1.79)	-0.003(1)	-0.01(12)	15000(144)	0.23

The resulting values of the fit parameters and the width of the flux tube that calculated from the Eq. 16 are displayed in the Table I. In this work, we did not converted our results into physical units and expressed the results in units of lattice
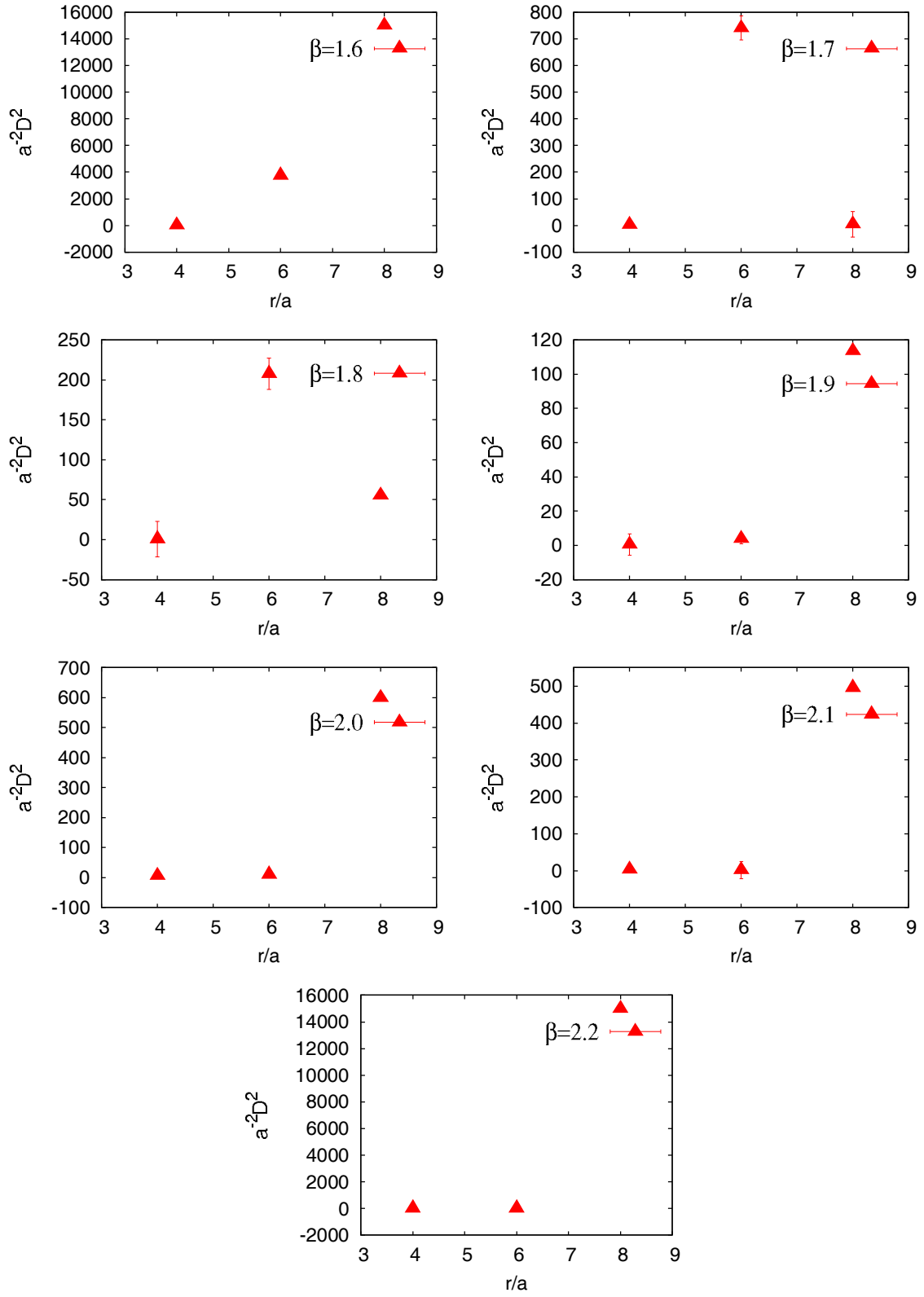
FIG. 5: The width of the flux tube as a function of the distance between the quark and the antiquark.
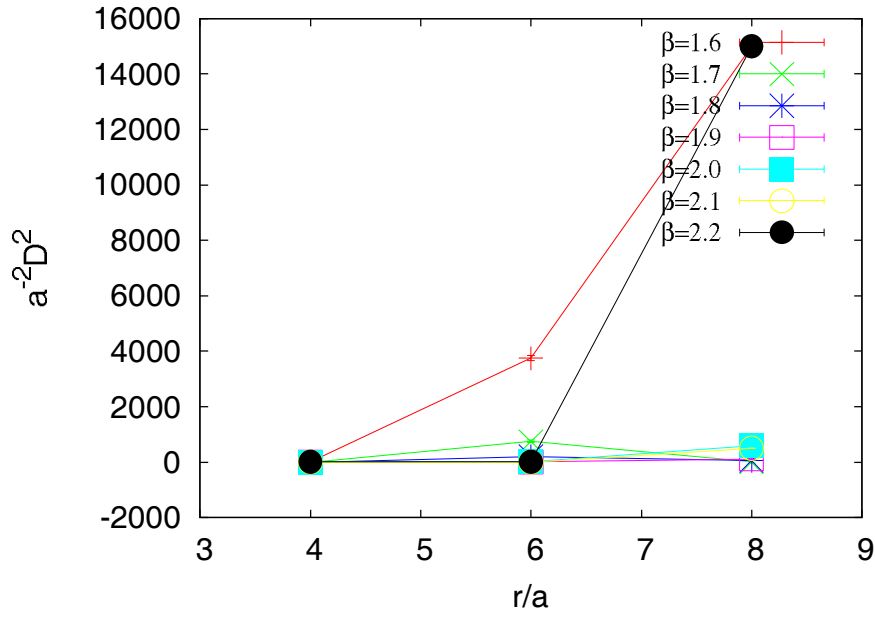
FIG. 6: The width of the flux tube as a function of the distance between the quark and the antiquark.
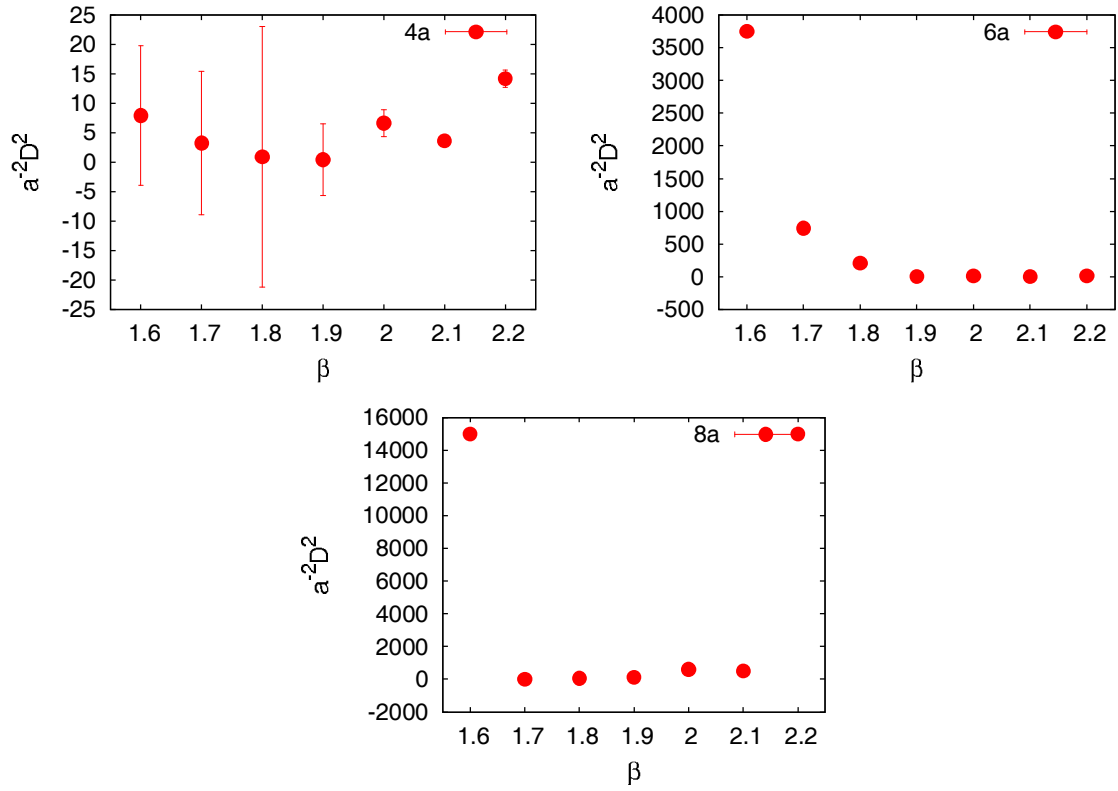

FIG. 7: The width of the flux tube as a function of the coupling constant.

spacing a. The width of the flux tube as a function of lattice $q\bar{q}$ separation for each

coupling constant is shown in Fig. 5. In Fig. 6, we plotted above all figures together in one plane. The width of the flux tube increases linearly depend on interquark distance, showed in [18]. From the two figures, our results coincide with the result of the work above generally.

We plotted the width of the flux tube as a function of the coupling constant for the values $r = 4a$, $6a$, $8a$ of the $q\bar{q}$ separation in Fig. 7. In Fig 8, we summarized graphics of the Fig. 7. According to the figures, small increase in the width observed at $\beta = 2.2$ for $r = 4a$ and one can say the width is stable from $\beta = 1.6$ to 2.1 then rises steeply when it reaches at $\beta = 2.2$ for $r = 8a$.
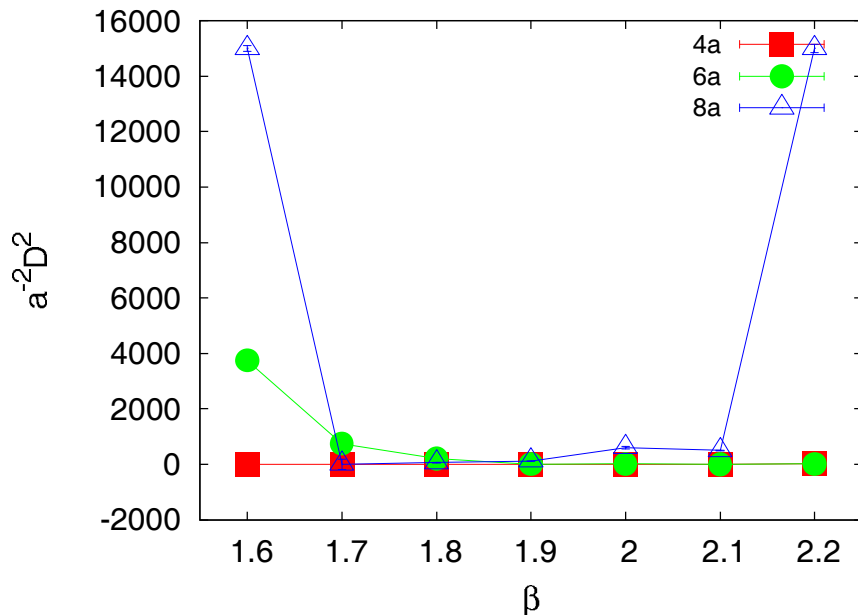
FIG. 8: The width of the flux tube as a function of the coupling constant.

V.   CONCLUSION

In this work, we investigated the dependence of the appearance and behaviour of the flux tube on the coupling constant and on the distance between two quarks at finite temperature in confined phase.

Since the configurations created by simulations have much fluctuations in lattice gauge theory at small value of β, our results have much statistical noises and was difficult to make any conclusion. However, we have tried to make the following conclusion.

Based on our results, we confirmed again that the width of the flux tube increases when the interquark distance increases. In the range of values of the coupling constants, the width of the flux tube is monotonic and it rises steeply at a certain values of the coupling constants. So, we concluded that the width of the flux tube diverges at finite temperature. This value was $\beta = 2.2$ for our case and in other words, for $N_\tau = 4$. The value of the coupling constant corresponds to $0.79T_c$. Therefore, $\beta = 1.9$ at zero temperature is different at finite temperature.

For further study, it is neccessary to perform simulations around the $0.79T_c$ on larger lattices. Also, we will determine string tension and its dependence on the coupling constant.

[1] O. Kaczmarek, F. Karsch, E. Laermann, and M. Lutgemeimer, Phys. Rev. **D62**, 034021 2000.

[2] O. Kaczmarek, F. Karsch, P. Petreczky, and F. Zantow, Phys. Rev. **D70**, 074505 2004.

[3] S. Chagdaa, Ph.D. thesis, Bielefeld University, 2008.

[4] S. Chagdaa, E. Laermann, G. Gombojav, and E. Galsandorj, Mongolian Journal of Physics 1, 33 2016.

[5] M. Creutz, *Quarks, Gluons and Lattices* (Cambridge university Press), 1983.

[6] N. Cardoso and P. Bicudo, Phys. Rev. **D85**, 077501 2012

[7] J.M. Drouffe, Nucl. Phys. **B170** [FS1], 91 1980.

[8] G. Munster and P. Weisz, Nucl. Phys. **B180** [FS2], 13 1981.

[9] G. Munster and P. Weisz, Nucl. Phys. **B180** [FS2], 330 1981.

[10] J. M. Drouffe and J. B. Zuber, Nucl. Phys. **B180** [FS2], 253 1981.

[11] J. M. Drouffe and J. B. Zuber, Nucl. Phys. **B180** [FS2], 264 1981.

[12] A. Hasenfratz, E. Hasenfratz, and P. Hasenfratz, Nucl. Phys. **B180** [FS2], 353 1981.

[13] G. Münster, Nucl. Phys. **B180** [FS2], 23 1981.

[14] M. Creutz, Phys. Rev. **D21**, 2308 1980.

[15] J. Langelage, G. Münster, and O.Phillipsen, PoS LAT2007:201,2007.

[16] G. Münster, Nucl. Phys. **B180** [FS2], 1 1981.

[17] R. Sommer, Nucl. Phys. **B306**, 181 1988

[18] A. Allais and M. Gaselle, Journal of High Energy Physics, JHEP 0901, 073 2009.

Discrete variable representation method calculation of the electronic structure of noble gas atoms

D. Naranchimeg[1], L. Khenmedekh[1], G. Munkhsaikhan[1], and N. Tsogbadrakh[2]*

[1]*Department of physics, Mongolian University of*

Science and Technology, Ulaanbaatar 14191, Mongolia

[2]*Department of physics, National University of Mongolia, Ulaanbaatar 14201, Mongolia*

We have been calculated ground state charge densities and energies of noble gas atoms through a single time dependent quantum fluid Schrödinger equation. By using imaginary - time, the Schrödinger equation has been transformed into diffusion equation. This equation numerically solved through discrete variable representation (DVR) method. Instead of the usual finite difference method the radial coordinate is discretized using the discrete variable representation constructed from Coulomb wave functions. Calculation was performed with use of Mathematica 7.0 programm.

I. INTRODUCTION

Numerical treatment of many - electron systems is extremely computationally demanding task. Density functional theory (DFT) calculation of many - electron systems is opened broad perspective for researchers. Though it uses only three coordinates, the number of equations to solve are increases with the number of electrons to be treated. Instead the quantum fluid density functional theory (QFDFT) solves only one time dependent generalized nonlinear Schrödinger equation (GNLSE) for many - electron systems. Using imaginary time for GNLSE, one could reach lowest energy state of the system, after tens of iterations.

GNLSE had been solved previously for calculation of ground state properties of noble gas atoms by finite difference method [1] and also by generalized pseudospectral method (GPSM) [2]. In the present study we used the Coulomb wave function discrete variable representation (CWDVR) method [3] for solution of the GNLSE for the noble

---

*Electronic address: Tsogbadrakh@num.edu.mn

gas atoms.

II.   THEORY AND METHODOLOGY

In this section we shall consider the numerical solution of the time - dependent Schrödinger equation for atomic systems to be

$$[-\frac{1}{2}\nabla^2 + v_{eff}(\rho)]\psi(\vec{r},t) = i\frac{\partial\psi(\vec{r},t)}{\partial t}. \tag{1}$$

The entire time - evolving interacting system is described by the complex - valued hydrodynamical wave function

$$\psi(\vec{r},t) = \rho(\vec{r},t)^{1/2}e^{i\chi(\vec{r},t)} = R(\vec{r},t)e^{i\chi(\vec{r},t)}. \tag{2}$$

However, one can write equation (1) in imaging time τ and substitute $\tau = -it$, t being the real time, to obtain, which closely resembles a diffusion - type equation:

$$[-\frac{1}{2}\nabla^2 + v_{eff}(\rho)]R(\vec{r},t) = -\frac{\partial R(\vec{r},t)}{\partial t} \tag{3}$$

$R(\vec{r},t)$ is the diffusion function and the diffusion process is governed by $v_{eff}(\rho)$. $v_{eff}(\rho)$ contains both classical and quantum potentials

$$v_{eff}(\rho) = v_{ee}(\rho) + v_{ne}(\rho) + v_{xc}(\rho) + v_{corr}(\rho) + v_{ext}(\rho) \tag{4}$$

The terms on the right - hand of Eq.(4) are as follows: the first is the inter - electron repulsion term, the second is the electron - nuclear attraction term, the third is exchange - correlation term, fourth term is the nonclassical correction, last term arises from interaction with the external field (in the present case, this interaction is zero).

III.   NUMERICAL SOLUTION: DVR METHOD

The diffusion equation (3) can be written as

$$[\hat{H}_0(\vec{r}) + \hat{V}(\vec{r},t)]R(\vec{r},t) = -\frac{\partial R(\vec{r},t)}{\partial t}. \tag{5}$$

We shall extend the second - order split - operator technique in spherical coordinates [4] for the time propagation of the Schrödinger equation:

$$R(\vec{r},t+\Delta t) \simeq e^{-\hat{H}_0\Delta t/2}e^{-\hat{V}(r,t+\Delta t/2)\Delta t}e^{-\hat{H}_0\Delta t/2}R(\vec{r},t) + O(\Delta t^3) \tag{6}$$

Here split operator technique is expressed in terms of $\hat{H}_0$, which is chosen to be the radial kinetic operator and $\hat{V}$ the remaining Hamiltonian. Matrix form of Hamiltonian operator is following:

$$[H]_{ij} = (D_2)_{ij} + V(x_i)\delta_{ij} \tag{7}$$

with

$$(D_2)_{ij} = \frac{1}{3}(E + \frac{Z}{x}), i = j \tag{8}$$

$$(D_2)_{ij} = \frac{1}{(x_i - x_j)^2}, i \neq j \tag{9}$$

The eigenvalues and eigenfunctions of $\hat{H}$ will be denoted as ε_k and ϕ_{ki}, respectively. The propagation of a given radial wave function $R(r,t)$ in order $\hat{H}$ can now be expressed as

$$[e^{-\hat{H}\Delta t/2}R(r,t)]_i = \sum_{j=1}^{N} S_{ij}R(r,t) \tag{10}$$

where

$$S_{ij} = \sum_k \phi_{ki}\phi_{kj}e^{-\varepsilon_k \Delta t/2}. \tag{11}$$

Note that S_{ij} is a complex symmetric matrix and it needs to be computed only once. The time propagation is therefore reduced to the matrix - vector product, which can be performed efficiently using the Mathematica 7.0 programm.

IV. RESULTS AND DISCUSSION

In this section we present results from nonrelativistic electronic structure calculations of the ground states of noble gas atoms. The main results for He, Ne and Ar atoms are suumarized in the Table I. Results from the calculations for the He atom are well agreed with the results from Roy [5] and HF [6]. However, in the case of Ne and Ar atoms differences in the total energies are obtained in our calculation, which is the result of the contribution of potential energy calculation.

Figure 1 represents the result of the calculation of the radial charge density distribution of Ne and Ar atoms. We note that the radial charge density calculated maintain the expected shell structure and closely resemble the HF density (not shown in the plot).

TABLE I: Calculated ground state properties of He, Ne and Ar(in au) along with literature data for comparison.

		He	Ne	Ar
-E	Present work	2.9000	128.9990	527.1320
	Roy[5]	2.8973	128.9065	527.5486
	HF[6]	2.8617	128.5470	526.8174
$-Z/r$	Present work	6.7878	311.115	1247.2100
	Roy[5]	6.7850	311.0597	1245.5699
	HF[6]	6.7492	311.1333	1255.0504
$1/r_{12}$	Present work	2.0678	65.7672	221.4480
	Roy[5]	2.0651	65.7129	220.6552
	HF[6]	2.0516	66.1476	231.6093
$-E_x$	Present work	1.0273	12.1128	29.5296
	exact	1.026	12.11	30.19
$-E_c$	Present work	0.0422	0.3561	0.7023
	Roy[5]	0.0423	0.3561	0.7011
T_w	Present work	-	94.2962	322.3100
	Roy[5]	-	94.2068	322.0345
	HF[6]	-	90.6140	308.4206
T_{corr}	Present work	-	34.7033	205.5490
	Roy[5]	-	34.7006	205.5177
	HF[6]	-	37.3886	214.4033

V.   CONCLUSIONS

The current research is focused on the results of the calculation of the electronic structure of the noble atoms. We describe the discrete variable representation method for the noble gas atoms. Results for noble gas atoms including effective potential, exchange and correlation contributions and ground state energy are presented and compared with calculated results from other researchers. For the next step of the research density functional theory with Kohn-Sham correction for ground state energy of noble gas atoms is going to be calculated.
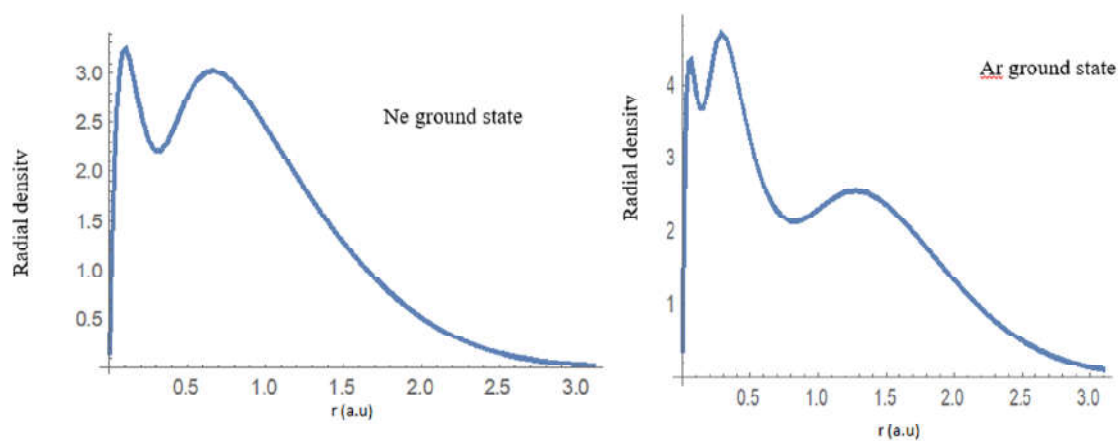
FIG. 1: The radial charge density distributions of ground state for Neon (left side) and Argon (right side) atoms

Acknowledgments

We have no interested the financial support.

[1] P. Hohenberg and W. Kohn, Phys. Rev. B **136**, 864 (1964).

[2] R. G. Parr and W. Yang, Density Functional Theory of Atoms and Molecules (New York: Oxford University Press) (1989).

[3] B. M. Deb and P. K. Chattaraj, Phys.Rev. A **39**, 1696 (1989).

[4] X. M. Tong and S. I. Chu, Chem.Phys.**217**, 119 (1997).

[5] A. K. Roy and S. I. Chu, J.Phys.B: At Mol.Opt.Phys. **35**, 2075 (2002).

[6] E.Clementi and C.Roetti, At.Data Nucl. Data Tables **14**, 174 (1974).

Few layers MoS$_2$ patterining by AFM nanolithography

G. Munkhsaikhan[1*], l. Ottaviano[2], m. Donarelli[3], s. Palleschi[2], f. Perozzi[2]

[*]*School of Applied Sciences, MUST, Bagatoiruu, Ulaanbaatar 14191, Ulaanbaatar, Mongolia*
[2]*Department of Physical and Chemical Sciences, University of L'Aquila, Via Vetoio 10, 67100, L'Aquila, Italy*
[3]*CNR-INO Brescia and Sensor Lab., Department of Information Engineering, University of Brescia, Via Branze 38, 25123, Brescia, Italy.*

This article aims to provide description on the development of atomic force microscopy (AFM) nanolithography for structuring and fabrication of few layers of MoS$_2$ at the nanometer scale. The bias-assisted AFM nanolithographic technique on mechanical exfoliated MoS$_2$ layers is reviewed. The reported AFM lithographic technique can be used to produce "artificial" edges, in few layers MoS$_2$ flakes and to exfoliate MoS$_2$.

I.   INTRODUCTION

The transition-metal dichalcogenides have received great attention because of its electronic, optical, and catalytic properties [1-3]. Among several TMDs, molybdenum disulfide has been investigated mostly because of its wide applications of thin-film transistors (TFTs), photodetectors, and energy storage. Thin film transistors based in single and few layers of MoS$_2$ that obtains fascinating properties as high on/off current ratio, high mobility at room temperature [4, 5].

The bulk MoS$_2$ crystal obtains 1.2 eV indirect band gap bulk phase, where 1.8 eV direct band gap corresponds to its exfoliated monolayer. These characteristics well satisfy with the nanoelectronic industry demands for two dimensional semiconductive materials. Many authors have reported interesting conductance properties and metallic behavior of MoS$_2$ edges and how they can be used as active sites for catalysis [6]. For these reasons, fabrication of "artificial" edges can be very useful for a new generation of

---

[1] gmunkhsaikhan@must.edu.mn

2D materials based nanodevices. However, this technique is realizable only in Ultra-High Vacuum (UHV) conditions with use of Scanning Tunneling Microscope (STM).

In this work, a new method to lithograph MoS$_2$ exfoliated flakes surfaces is investigated that performed in air, with a setup similar to the LAO one.

II.   METHODOLOGY AND EXPERIMENTAL DETAILS

A.   Mechanical Exfoliated single and few layers of MoS$_2$

At the first step, we start on mechanical exfoliation method to prepare samples. Mechanical exfoliation is the simple and best method known as "scotch-tape", based on the isolation of mono and many MoS$_2$ layers from bulk ones [7]. MoS$_2$ crystal (SPI supplies, CAS 1317-33-5) has been exfoliated by micromechanical technique, with a scotch tape. The exfoliated MoS$_2$ flakes have been deposited on heavily doped silicon substrates (resistivity 0.01 $\Omega \cdot$cm). Next step, our research is focused on identification of mechanically exfoliated few layer MoS$_2$ via optical microscopy. It is known that clear optical contrast is obtained by selecting a proper substrate, silicon wafer covered with SiO$_2$ layer on top of it. However, since we have used conductive Si substrate we have faced problem of obtaining suitable optical contrast. Only many layers of MoS$_2$ were merely were appeared in the white contrast, where identification of mono- or few layers became almost impossible. A new approach so called "blindly seeking method" is used in this investigation. Here, for an identification of less contrast area (possibly few layers) we recommend to perform a simultaneous AFM investigation near this region. By obtaining few layers we mark position coordination of this area for future lithography process.

B.   AFM lithography of MoS$_2$

The size of the deposited MoS$_2$ flakes have been analyzed by Atomic Force Microscopy (AFM Digital D5000, Veeco). The same Atomic Force Microscope has been used to lithograph the flakes. The lithography process is similar to the one adopted for LAO. A conductive AFM tip (cantilever resistivity 0.01-0.025 $\Omega \cdot$cm, antimony n-doped silicon, tip radius about 10 nm) has been biased at negative voltages (ranging from -8 V to -12 V), and kept at 10 nm from the surface. The silicon substrate has been grounded.

III. RESULTS

A sketch of the lithography technique is reported in Figure 1, upper-right inset. The lithographic process is performed in air (relative humidity about 50%, temperature about 20 °C), where a water meniscus is formed between tip and sample. The applied voltage caused the migration of water H^+ ions to the conductive tip, while the OH^- ions are pushed onto the MoS_2 surface. The tip has scanned the region one wanted to lithograph, through an automated system. After that, the lithographed sample has been rinsed in a 0.1 M HCl solution, in order to remove the lithographed regions of the MoS_2 surface [8].
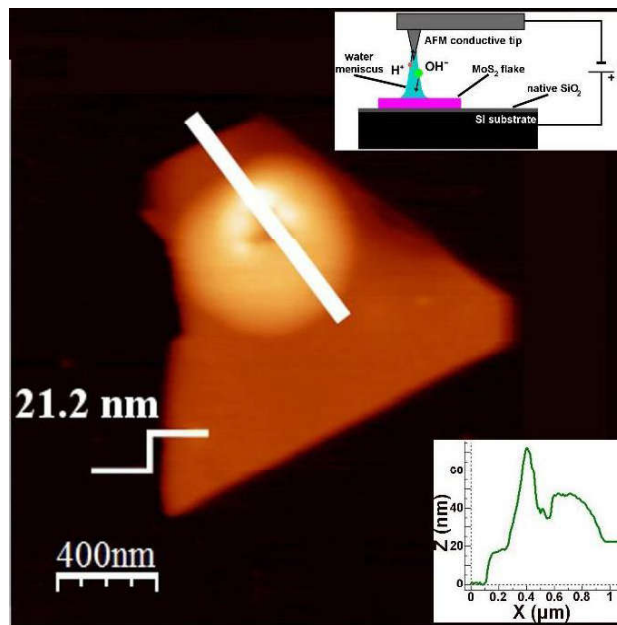

FIG. 1: AFM image of a lithographed MoS_2 flake, the white line represents the lithography path. Height and line profile of the lithographed region are reported in the bottom-right inset. Upper-right inset: sketch of the setup used for nanolithography [8].

The lithographed and chemically etched flakes have been studied by Donarelli et all, where X-ray Photoelectron Emission Microscopy (XPEEM) using the end-station of the NanoESCA beamline of Elettra synchrotron radiation facility. The experimental set-up includes a non-magnetic, electrostatic PEEM and a double-pass hemispherical analyzer. To analyze the flakes, spatially resolved XPS is mandatory, being the lateral dimensions of the flakes of the order of 1 μm, and the features related to the lithography process of the order of hundreds of nm. In the present experiment the NanoESCA microscope was

operated with a spatial resolution of ~100 nm calculated from the used contrast aperture size in the PEEM column. In addition to imaging spectroscopy the NanoESCA end-station also provides an operational mode to obtain fast XPS spectra from a sample [8].

An AFM image of a lithographed flake is reported in Figure 2. The brighter region of the image is the one affected by the lithography process. To lithograph the flake, the AFM tip has been biased at -8 V (the sample has been grounded) and it has scanned the flake along the white line (superimposed at the AFM image) at 0.1 μm/s speed. The height of the lithographed region, taken along the white line, is reported in the middle of Figure 2. The height is quite uniform along the path, and it reaches the value of about 17 nm. The height of the flake (recorded in the not-lithographed area) is 12.2 nm, i.e. 17 MoS$_2$ layers. After that, the lithographed sample has been rinsed in a 0.05 M HCl solution, in order to remove the lithographed regions of the MoS$_2$ surface for 10 seconds. The chemical etching has removed the lithographed region, creating 6.8nm depth hole in the flake. Therefore, the AFM lithography is capable to fabricate artificial edges in MoS$_2$ exfoliated flakes.
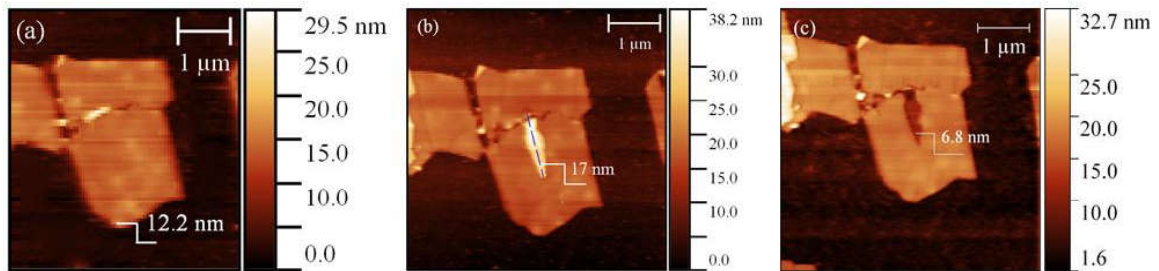

FIG. 2: AFM image of a lithographed MoS$_2$ flake, the white line represents the lithography path. Height and line profile of the lithographed region are reported.

As can be seen in Figure 2, after AFM biased tip and chemical etching of MoS$_2$, the upper region of the lithographed flake is not completely removed: just the uppermost layers have been etched (the lithographed area, recognizable in panel (b), does not correspond to the hole). So, the described nanolithography process can also be used to further exfoliate the flakes.

An AFM image of the thinnest lithographed flake with 9.8nm height is shown in Figure 3. The bright dashed line region of the image is the one affected by the lithography process. To lithograph the flake, the AFM tip has been biased at -7 V and it has scanned the flake along the white line at 0.1 μm/s speed. Here, a scratched hole along

the white line is occurred, in the middle of Figure 3. The lithographed sample has been rinsed in a 0.05 M HCl solution, where 2.5nm depth hole is created in the flake. The height of the flake after lithography has reduced to 8.5 nm, which likely shows that MoS_2 layers can be exfoliated by the lithography technique.
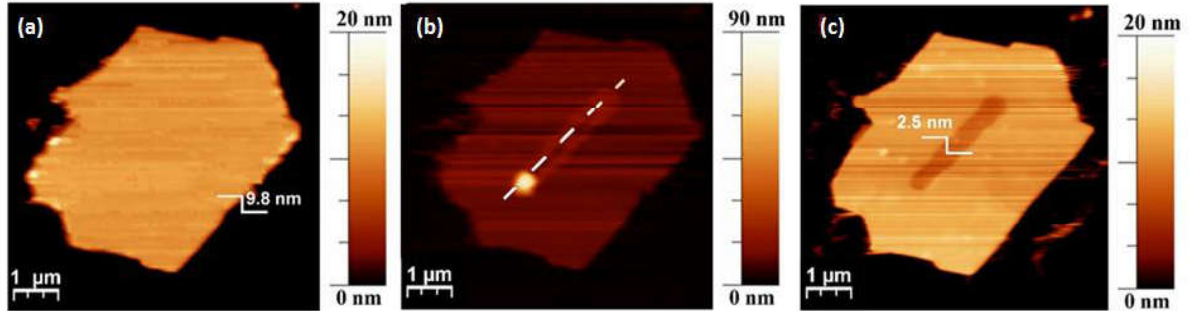

FIG.3: Panel (a): AFM image of the thinnest MoS_2 flake before nanolithography. Panel (b): AFM image of the MoS_2 flake after nanolithography process (Vtip= -7 V, vtip= 0.1 μm/s). Panel (c): AFM image of the MoS_2 flake after selective chemical etching (HCl solution, 0.05 M).

IV. SUMMARY

In this work, a new technique to lithograph the MoS_2 flakes at the nanometer scale is reported. The importance of this technique is demonstrated by AFM measurements. The experimental setup is similar to the well-established LAO. However the lithography technique is not based on the oxidation of the surface. On the other hand, the same measurements indicate a sulfur desorption likely induced by an OH^- ions "bombardment" of the molybdenite surface. The here reported lithographic technique can be used to fabricate "artificial" edges on MoS_2 flakes. Furthermore, AFM lithographic technique can be used also to exfoliate MoS_2.

[1]. Lembke D, Bertolazzi S, Kis A (2015). Single-layer MoS_2 electronics. Acc Chem Res 48:100−110.

[2]. Xia F, Wang H, Xiao D, Dubey M, Ramasubramaniam A (2014) Two-dimensional material nanophotonics. Nat Photon 8:899−907.

[3]. Bonaccorso F, Colombo L, Yu G, Stoller M, Tozzini V, Ferrari AC, Ruoff RS, Pellegrini V (2015) Graphene, related two-dimensional crystals, and hybrid systems for energy conversion and storage. Science 347:1246501

[4]. Radisavljevic B, Radenovic A, Brivio J, Giacometti V, Kis A (2011) Single-layer MoS$_2$ transistors. Nat. Nanotechnol 6:147–50.

[5]. Kim S, Konar A, Hwang WS, Lee JH, Lee J, Yang J, Jung C, Kim H, Yoo JB, Choi JY, Jin YW, Lee SY, Jena D, Choi W, Kim K (2012) High-mobility and low-power thin-film transistors based on multilayer MoS$_2$ crystals. Nat Commun 3:1011

[6]. M.V. Bollinger, J.V. Lauritsen, K.W. Jacobsen, J.K. Nørskov, S. Helveg and F. Besenbacher, Phys. Rev. Lett., 2001, 87, 196803.

[7]. Novoselov, K. S.; Geim, A. K.; Morozov, S. V.; Jiang, D.; Zhang, Y.; Dubonos, S. V.; Grigorieva, I. V.; Firsov, A. A., Electric field effect in atomically thin carbon films. Science 2004, 306 (5696), 666- 669.

[8]. M. Donarelli et all. Few layered MoS$_2$ lithography with an AFM tip: description of the technique and nanospectroscopy investigations. Nanoscale, Issue 26, 2015

Nanocrystal microstructure and phase transformation of rare earth element neodymium(nd) substituted NiTi shape memory alloys

M.Dovchinvanchig [1], D.Sangaa[2], C.W.Zhao[3],

[1] *Department of Matematics, Physics and Information Technology, School of Engineering and Technology, Mongolian Univesity Life Science Ulaanbaatar, Mongolia*

[2]*Institute of Physics and Technology, Mongolian Academy Sciences*

[3]*College of Art and Science, Shanghai Maritime University, Shanghai China*

The substitutional effect of rare earth element neodymium (Nd) on the crystal structure microstructure and phase transformation behavior of $Ni_{50}Ti_{50-x}Nd_x$ (x= 0, 0.1, 0.3, 0.5, 0.7 at.%) shape memory alloy was investigated by scanning electronic microscope, X-ray diffraction and differential scanning calorimetry. The microstructure analyses reveal that Ni-Ti-Nd ternary alloy contains three phases: NiNd, $NiTi_2$ and NiTi matrix. A one-step martensitic transformation is observed in the alloys. The martensitic transformation temperature *Ms* increases sharply with increasing content of Nd.

I. INTRODUCTION

Nearly equiatomic Ni-Ti shape memory alloys (SMAs) have remarkable shape memory effects and excellent mechanical properties and have been used in various fields, particularly in engineering and medical application in aerospace, electron actuators, smart material, coupling and including pipeline joints[1]. Current research interest on SMAs mainly lies in controlling the martensitic transformation temperature and improving the shape memory effect for their applications. The effects of martensitic transformation, super-elasticity, and shape memory effect have been widely studied by adding transitional elements to Ni-Ti binary alloys as elements like Fe [2], Hf [3], Pd [4] and etc. It is found that most alloying elements for example Fe lower martensitic transformation temperature; and only a few elements, such as Hf, Pd increase martensitic transformation temperature [5].

Moreover, the microstructure and martensitic transformation temperature of the rare earths RE= Ce [6], Gd [7], Dy [8], La [9] addition to Ni-Ti binary alloys have also been studied using scanning electron microscopy (SEM), energy dispersive spectrometry (EDS), X-ray diffraction (XRD), and differential scanning calorimetry (DSC). It was found, that the addition of these REs to Ni-Ti binary alloys increases the martensitic transformation temperature and changes the phase transformation sequence.

Rare earth element Nd is also a widely used element, particularly in magnetic materials. However, only few studies have been conducted on Nd substituition to shape memory alloy. So far in the literature is known which reports Nd substitution range between 1 at.% to 20 at.% to Ni-Ti alloy[10]. However the effect of Nd addition to Ni-Ti binary alloy on microstructure and martensite transformation temperature remained unclear.

Here, in this paper, Nd content was varied; 0.1%, 0.3%, 0.5%, 0.7% atomic fraction of Nd was added to Ni-Ti binary alloys, and the microstructure and martensitic transformation were studied experimentally.

II. EXPERIMENTS

The $Ni_{50}Ti_{50-x}Nd_x$ alloys were prepared by melting each 10 g of mixture of starting materials with different nominal compositions (99.9 mass % sponge Ti, 99.7 mass % electrolytic Ni and 99.95 mass % Nd) in a non-consumable arc-melting furnace using a water-cooled copper crucible. The alloys are denoted by Nd0, Nd0.1, Nd0.3 Nd0.5 and Nd0.7 to refer to $Ni_{50}Ti_{50}$, $Ni_{50}Ti_{49.9}Nd_{0.1}$, $Ni_{50}Ti_{49.7}Nd_{0.3}$, $Ni_{50}Ti_{49.5}Nd_{0.5}$ and $Ni_{50}Ti_{49.3}Nd_{0.7}$ alloys, respectively. Arc-melting was repeated four times to ensure the uniformity of composition. The specimens are spark-cut from the ingots and heat treated at 850 °C for an hour in a quartz tube furnace. Subsequently the specimens were quenched using water. Thereafter, the specimens are mechanically and lightly polished to obtain a plain surface.

The phase transformation temperatures of $Ni_{50}Ti_{50-x}Nd_x$ alloys were determined by DSC using a TA Q2000 calorimeter. The temperature range of heating and cooling was from -30 °C to 150 °C, and the scanning rate of heating and cooling was 10 °C/min. SEM observations were conducted using a FEI Quanta 650 FEG equipped with EDS analysis system by Oxford Instruments. An XRD experiment was conducted using a D/MAX-2500PC X-ray diffractometer.

III.   RESULTS AND DISCUSSION

Microstructure of Ni$_{50}$Ti$_{50-x}$Nd$_x$ alloy

Fig. 1a depicts the XRD curves of Ni$_{50}$Ti$_{50-x}$Nd$_x$ (x=0, 0.1, 0.3, 0.5, 0.7) alloys at room temperature. The diffraction peaks are identified to be from NiTi B19' martensite phase, NiTi B2 austenite phase, NiTi$_2$ phase and NiNd alloy after comparing with JCPDF cards (. 65-0145, 65-4572, 72-0442, and 19-0818). The detailed crystal plane indices are marked in Fig.1c for Nd0.1 and Fig.1d for Nd0.7, but the relative intensities of each XRD pattern are quite different because of the differences in martensite phase fraction and austenite phase fraction. In this paper, the letter M denotes the NiTi B19' martensite phase and the letter A denotes the NiTi B2 austenite phase. This result is confirmed in the following DSC analysis. Fig. 1b depicts a comparison of martensitic diffraction peaks of Ni$_{50}$Ti$_{50-x}$Nd$_x$ (x=0, 0.1, 0.3, 0.5, 0.7) alloys. It is seen that the martensitic peak the diffraction angle decreases with increasing Nd fraction. It indicates that the lattice of the martensite expands with Nd addition.
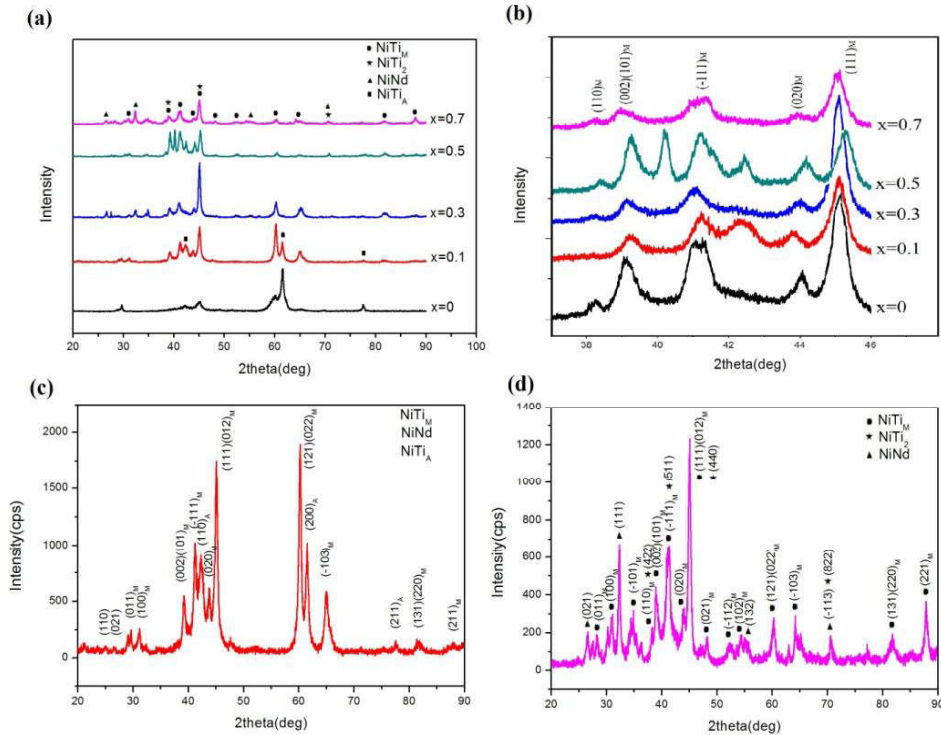

FIG. 1: XRD curves of Ni$_{50}$Ti$_{50-x}$Nd$_x$ alloys:
(a) XRD curves of Ni$_{50}$Ti$_{50-x}$Nd$_x$ alloys; (b) comparison of martensitic diffraction peaks of Ni$_{50}$Ti$_{50-x}$Nd$_x$ alloys; (c) Indexed diffraction peaks in Nd0.1; (d) Indexed diffraction peaks in Nd0.7;

The lattice parameters of alloys can be also calculated by peak position in XRD patterns and shown in Table 1. It is shown clearly that the cell volume V expand for either martensite or austenite with Nd addition to Ni-Ti binary alloy from 0 at. % to 0.7 at. %. The observation can also be confirmed in the following composition analysis.

Table 1 Lattice parameters of Ni-Ti-Nd alloys

Alloy	Phase	a(nm)	b(nm)	c(nm)	β(°)	V(nm^3)	Source
Nd0	M	0.2898	0.4121	0.4619	97.86	0.05464	
Nd0.1	M	0.28824	0.41324	0.46307	97.36	0.05470	
	A	0.30148					
Nd0.3	M	0.28925	0.41211	0.46425	97.62	0.05484	
Nd0.5	M	0.28933	0.41350	0.46472	97.67	0.05510	
Nd0.7	M	0.28999	0.41418	0.46635	97.85	0.05548	
NiTi	M	0.2898	0.4108	0.4646	97.78	0.05480	JCPDF card No.65-0145
	A	0.3007				0.02719	JCPDF card No.65-4572
NiTi$_2$		1.131				1.4503	JCPDF card No.72-0442
NiNd		0.3803	1.046	0.4339		0.17262	JCPDF card No.19-0818

Morphologies and compositions of Ni$_{50}$Ti$_{50-x}$Nd$_x$ alloys

Fig. 2 depicts the back-scattering SEM images of Ni$_{50}$Ti$_{50-x}$Nd$_x$ (x=0, 0.1, 0.3, 0.5, 0.7) alloys. For Nd0 alloy, there is only one phase that can be identified in the SEM image (Fig.2a). For Nd0.1 and Nd0.3, two different phases, namely, matrix and a bright phase, can be identified in the SEM images (Fig.2b-c). Some bright particles that are nearly round-shape and up to 3 μm and 7 μm in diameter, respectively, are distributed randomly in the matrix. In addition, the bright phase is found on grain boundaries of the matrix. For Nd0.5 and Nd0.7, three different phases, namely, a bright phase, a dark phase and the matrix, can be identified in the SEM images (Fig.2d-e). Bright particles

that are nearly round-shape and up to 18 µm and 25 µm in diameter, respectively, are distributed randomly in the matrix, together with some larger, curved particles . The dark phase is in irregular shape and distributed randomly in the matrix. The size of the bright particles and the volume fraction of the bright phase increases with increasing Nd fraction.
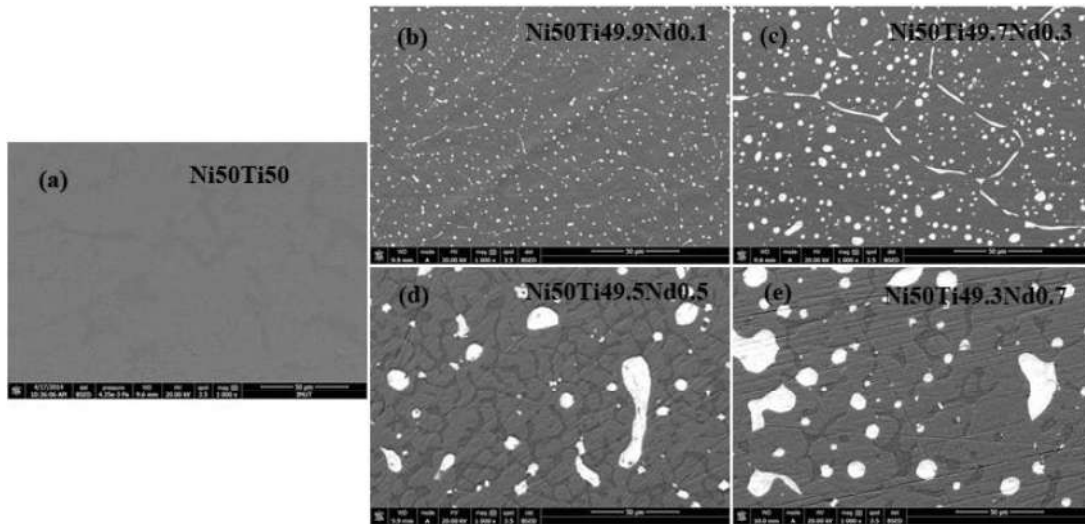

FIG. 2: Back-scattering SEM images of $Ni_{50}Ti_{50-x}Nd_x$ alloys:
(a) $Ni_{50}Ti_{50}$; (b) $Ni_{50}Ti_{49.9}Nd_{0.1}$; (c) $Ni_{50}Ti_{49.7}Nd_{0.3}$; (d) $Ni_{50}Ti_{49.5}Nd_{0.5}$; (e) $Ni_{50}Ti_{49.3}Nd_{0.7}$

To identify the phases, EDS analysis was conducted in SEM. The compositions of Ni-Ti-Nd alloys are shown in Table 2. The Ti:Ni ratio in the matrix of all Ni-Ti-Nd alloys is measured to be close to 1. The Ti:Ni ratio in the dark phase of Nd0.5 and Nd0.7 alloy is measured to be nearly 2:1. By XRD analysis, there is a $NiTi_2$ phase in Nd0.5 and Nd0.7. Thus, the dark phase can be concluded to be $NiTi_2$ phase. According to the 773 K isothermal section of the ternary alloy phase diagram of the Ni-Ti-Nd, no intermetallic compounds can be found in the Ti-Nd binary system. However, the Ni-Nd binary alloy phase diagram shows seven intermetallic compounds defined as $NdNi_5$, Nd_2Ni_7, $NdNi_3$, $NdNi_2$, $NdNi$, Nd_7Ni_{13}, and Nd_3Ni [12]. The EDS results show that the Ni:Nd ratio in the bright phase is nearly 1 and can be regarded as the NiNd intermetallic compound with a small amount of Ti solute.

Tabel 2 Compositions of Ni-Ti-Nd alloys

Alloy	Phase	Ti (at. %)	Ni (at. %)	Nd (at. %)
Nd0	matrix	49.1	50.9	0
Nd0.1	matrix	50.5	49.5	0
	bright phase	3.6	49.2	47.2
Nd0.3	matrix	50.7	49.3	0
	bright phase	3.7	48.9	47.4
Nd0.5	matrix	50.7	49.3	0
	bright phase	3.2	49.0	47.8
	dark phase	66.7	33.3	0
Nd0.7	matrix	51.0	49.0	0
	bright phase	4.0	49.0	47.0
	dark phase	66.4	32.9	0.7

Furthermore, Nd has also been found in the dark phase of Nd0.7. The Nd atomic radius (0.206nm) is larger than Ti atomic radius (0.176nm) by 17% and Ni atomic radius (0.149nm) by 38% [13]. The Nd atom occupies the position of Ni or Ti, consequentially resulting in an expansion of the Ni-Ti-based matrix lattice [7], which is consistent with the XRD analysis.

Phase transformation of $Ni_{50}Ti_{50-x}Nd_x$ alloys

Fig. 3a depicts the DSC curves of the $Ni_{50}Ti_{50-x}Nd_x$ (x=0, 0.1, 0.3, 0.5, 0.7) alloys. Each DSC curve of Nd0, Nd0.1, Nd0.3, Nd0.5, and Nd0.7 shows only one peak during the heating and cooling process, which indicates a one-step B2↔B19' phase transformation. Fig. 3b shows the effect of Nd concentration on martensitic transformation start temperature M_s. For Nd0 alloy, the M_s is measured to be 77.44 °C. It is well known that quenched Ti-Ni alloys show one-step B2↔B19' transformation and the transformation temperatures are strongly dependent on Ni concentration [5, 7]. 0.1 at. % increase in Ni concentration can lower the M_s of Ti–Ni alloy by more than10 °C. For example, Liu *et al* measured the M_s to be about -50 °C for $Ni_{50.7}Ti_{49.3}$ alloy after annealing at 900 °C for 60min [7]. Tabish *et al* measured the M_s to be -22.12 °C for $Ni_{50}Ti_{50}$ alloy after annealing at 1000 °C for 120min [14]. Wasilewski *et al* measured

the M_s to be 65 °C for $Ni_{49.8}Ti_{50.2}$ alloy [15]. In this work, the composition of the matrix in Nd0 is $Ni_{49.36}Ti_{50.64}$, which is Ti-rich. So, the M_s of Ti–Ni binary alloy Nd0 is reasonable. Meanwhile, the martensite transformations finish temperature M_f in Nd0 alloy is higher than room temperature of 20 °C. Thus, the martensite transformations have finished at room temperature and the Nd0 alloy should be composed of pure martensite phase, which is in agreement with the XRD results.

Fig. 3 shownns the M_s increases with increasing Nd fraction from 0.1 at. % to 0.7 at. %. And, all M_f in four DSC curves of Nd addition alloys, are lower than room temperature. Thus, martensite transformation cannot finish fully at room temperature, which indicates that both the austenite phase and the martensite phase exist in the Ni-Ti-Nd alloy.
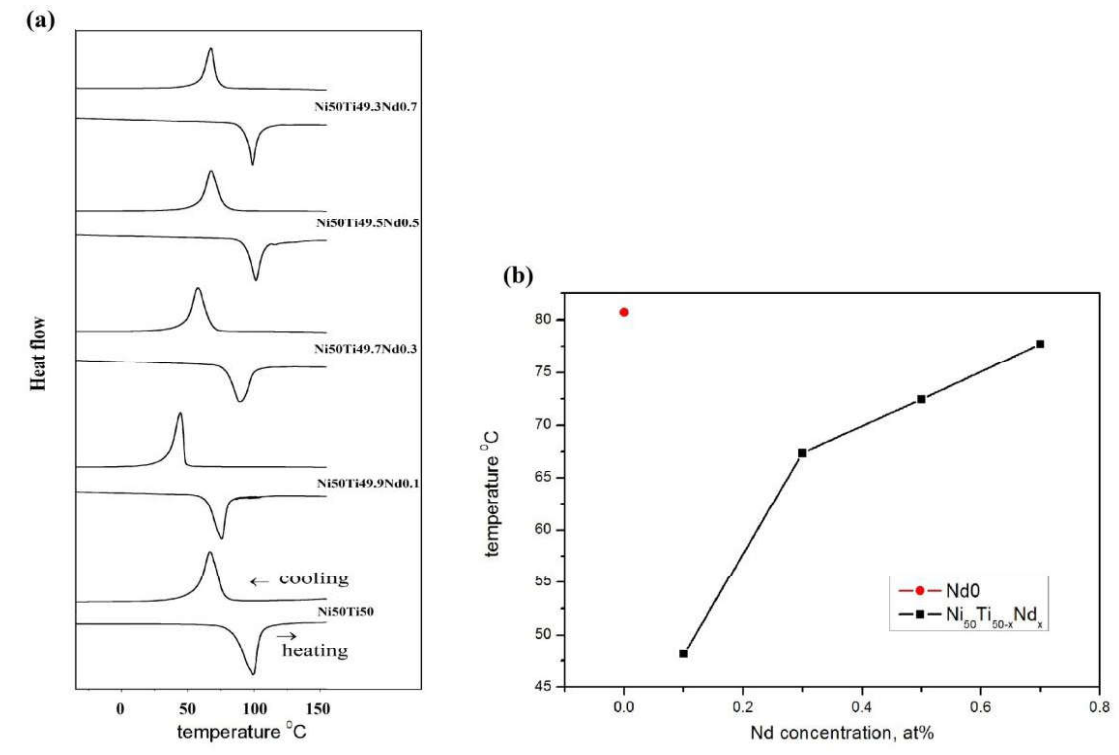

FIG. 3: DSC curve and martensite transformation temperature of $Ni_{50}Ti_{50-x}Nd_x$ alloys: (a) DSC curves; (b) M_s curve

IV. CONCLUSION

In summary, the effect of rare earth element Nd addition on the microstructure and martensitic transformation behavior was investigated by XRD, SEM and DSC. The microstructure of the $Ni_{50}Ti_{50-x}Nd_x$ alloys consists of Ni-Nd alloy with a small amount

of Ti solute and Ni-Ti matrix. The lattice of Ni-Ti-based matrix is expanded by Nd addition. The Ni-Ti-Nd alloy shows a one-step martensitic transformation. Increasing the Nd fraction, the martensitic transformation start temperature M_s increases.

[1]. K. Otsuka, and X. Ren, "Recent developments in the research of shape memory alloys," Intermetallics, vol. 7, no. 5, pp. 511-528, 1999.

[2]. J. Frenzel, J. Pfetzing, K. Neuking, et al, "On the influence of thermomechanical treatments on the microstructure and phase transformation behavior of Ni-Ti-Fe shape memory alloys," Mat. Sci. Eng. A, vol. 482-484, pp. 635-638, 2008.

[3]. X.L. Meng, W. Cai, Y.D Fu, et al, "Shape memory behaviors in an aged Ni-rich TiNiHf high temperature shape-memory alloy," Intermetallics, vol. 16, no. 5, pp. 698-705, 2008.

[4]. Y. Liu, M. Kohl, K. Okutsu, et al, "TiNiPd thin film microvalve for high temperature applications," Mat. Sci. Eng. A, vol. 378, no. 1-2, pp. 205-209, 2004.

[5]. K. Otsuka, X. Ren, "Physical metallurgy of Ti-Ni-based shape memory alloys," Prog. Mater. Sci., vol. 50, no. 5, pp.511-678, 2005.

[6]. W. Cai, A.L. Liu, J.H. Sui, L.C. Zhao, "Effects of Cerium Addition on Martensitic Transformation and Microstructure of Ti49:3Ni50:7 Alloy," Mater. Trans., vol.47, no. 3, pp. 716-719, 2006.

[7]. A.L. Liu, W. Cai, Z.Y. Gao, et al, "The microstructure and martensitic transformation of $(Ti49.3Ni50.7)_{1-x}Gd_x$ shape memory alloys," Mat. Sci. Eng. A, vol.438-440, pp. 634-638, 2006.

[8]. A.L. Liu, Z.Y. Gao, L. Gao, W. Cai, Y. Wu, "Effect of Dy addition on the microstructure and martensitic transformation of a Ni-rich TiNi shape memory alloy," J. Alloy Compd. vol.437, no.1-2, pp.339-343, 2007.

[9]. J.W. Xu, A.L. Liu, B.Y. Qian, W. Cai, "Investigation on Microstructure and Phase Transformation of La added TiNi Shape Memory Alloy," Adv. Mater. Res. vol.557-559, pp.1041-1044, 2012.

[10]. M.Dovchinvanchig, C.W.Zhao, S.L.Zhao, X.K.Meng, Y.J.Jing, Y.M.Xing "Effect of Nd Addition on the Microstructure and Martensitic Transformation of Ni-Ti Shape Memory Alloys," Adv. in Mater. Sci and Eng., vol. 2014, article ID 489701,

2014.

[11]. J.W. Xu, A.L. Liu, W. Cai, "Crystal structure and formation mechanism of rare earth rich phases in Ti-Ni-Ce alloys," J. Funct. Mater., vol.39, no.4, pp. 600-602, 2008.(in Chinese)

[12]. J.Q. Liu, Y.H. Zhuang, Y.Q. Hu, "The 773K Isothermal section of the ternary phase diagram of the Nd-Ni-Ti," J. Alloy Compd., vol. 368, no. 1-2, pp. 180-181, 2004.

[13]. E. Clementi, D.L. Raimondi, W.P. Reinhardt, "Atomic screening constant from SCF functions. II. Atoms with 37 to 86 electrons," J. Chem. Phys., vol.47, no.4, pp.1300-1307, 1967.

[14]. T.A. Tabish, S. Atiq, M. Ali, A.N. Ch, Z.U. Reham, T.Z. Butt, "Development and characterization of $Ni_{50}Ti_{50}$ shape memory alloy used for biomedical applications," Int. J. Chem Mater. Sci. Eng., vol. 7, no. 12, pp. 92-93, 2013.

[15]. R.J. Wasilewski, S.R. Butler, J.E. Hanlon, "On the Martensitic Transformation in TiNi," Met. Sci. J., vol. 1, pp. 104-110, 1967.